A delta-tubulin/epsilon-tubulin/Ted protein complex is required for centriole architecture

Rachel Pudlowski[1], Lingyi Xu[1], Ljiljana Milenkovic[2], Chandan Kumar[1], Katherine Hemsworth[1], Zayd Aqrabawi[1], Tim Stearns[2,3], Jennifer T. Wang[1,*]

1 - Department of Biology, Washington University in St. Louis
2 - Department of Biology, Stanford University
3 - Rockefeller University
* - Corresponding author

Abstract

Centrioles have a unique, conserved architecture formed by three linked “triplet” microtubules arranged in nine-fold symmetry. The mechanisms by which these triplet microtubules are formed are not understood and likely involve the noncanonical tubulins delta-tubulin and epsilon-tubulin. Previously, we found that human cells deficient in delta-tubulin or epsilon-tubulin form abnormal centrioles, characterized by an absence of triplet microtubules, lack of central core protein POC5, and a futile cycle of centriole formation and disintegration (Wang et al., 2017). Here, we show that human cells lacking either of the associated proteins TEDC1 and TEDC2 have these same phenotypes. Using ultrastructure expansion microscopy, we find that mutant centrioles elongate to the same length as control centrioles in G2-phase. These mutants fail to recruit inner scaffold proteins of the central core and have an expanded proximal region. During mitosis, the mutant centrioles elongate further before fragmenting and disintegrating. All four proteins physically interact and TEDC1 and TEDC2 are capable forming a subcomplex in the absence of the tubulins. These results support an AlphaFold Multimer model of the tetramer in which delta-tubulin and epsilon-tubulin are predicted to form a heterodimer. TEDC1 and TEDC2 localize to centrosomes and are mutually dependent on each other and on delta-tubulin and epsilon-tubulin for localization. Our results demonstrate that delta-tubulin, epsilon-tubulin, TEDC1, and TEDC2 function together to promote robust centriole architecture. This work also lays the groundwork for future molecular studies of this complex, providing a basis for determining the mechanisms that underlie the assembly and interplay between the triplet microtubules and inner centriole structure.

Introduction

The major microtubule organizing center of mammalian cells, the centrosome, is composed of two barrel-shaped centrioles surrounded by layers of pericentriolar material (Breslow and Holland, 2019). The unique architecture of the centriole is highly conserved: the centriole barrel walls of approximately 250 nm in diameter by 500 nm in length are formed of compound microtubules linked to each other through shared protofilament walls, arranged in nine-fold symmetry (Wang and Stearns, 2017). Centrioles exhibit proximal-distal polarity comprised of three subdomains: the proximal end with triplet microtubules, the distal end with doublet microtubules, and the central core spanning the two regions (LeGuennec et al., 2021). The triplet microtubules are named the A-, B-, and C-tubules. The A-tubule is a complete microtubule formed of 13 protofilaments, and the B- and C-tubules are partial tubules and share protofilament walls with adjacent tubules. The A- and B-tubules extend beyond the C-tubule to form the doublet microtubules of the centriole distal end. During ciliogenesis, the A- and B-tubules elongate further to form the ciliary axoneme (Wang and Stearns, 2017).

Compound microtubules are unique to centrioles and ciliary axonemes and are conserved in almost all organisms with these organelles. Little is known about the mechanisms by which they form, or the functional roles they play within centrioles and cilia. Two non-canonical members of the tubulin superfamily, delta-tubulin (TUBD1) and epsilon-tubulin (TUBE1), are required for compound microtubule formation or stability in multiple organisms (de Loubresse et al., 2001; Dupuis-Williams et al., 2002; Dutcher and Trabuco, 1998; Dutcher et al., 2002; Gadelha et al., 2006; Goodenough and StClair, 1975; Ross et al., 2013; Wang et al., 2017). Previously, we showed that human cells lacking these tubulins make aberrant centrioles that only have singlet microtubules and disintegrate in mitosis, resulting in a futile cycle of centriole formation and loss every cell cycle (Wang et al., 2017). These mutant centrioles fail to recruit the distal end protein POC5, indicating that compound microtubules may be required for centriole composition. We concluded that either the compound microtubules themselves, or the proteins that they associate with, are required for centriole stability through the cell cycle. Together, these results suggest that the compound microtubules may form a unique scaffold for the protein-protein interactions that define centrosomes and cilia.

The compound microtubules are directly linked to many of the substructures at the proximal, central, and distal regions within centrioles. At the proximal end, the cartwheel, a ninefold symmetric hub and spokes made from SASS6 and associated proteins, is connected to the A-tubule through the pinhead, which has been proposed to be formed of CEP135 and CPAP (Hatzopoulos et al., 2013; Kraatz et al., 2016; Lin et al., 2013a; Sharma et al., 2016). Multiple cartwheels are stacked within the centriole lumen to a height of approximately one-third of the entire centriole length (~170 nm in human centrioles) (Klena et al., 2020). The A-tubule of one triplet is connected to the C-tubule of the adjacent triplet through a structure known as the A-C linker. Recently CCDC77, WDR67, and MIIP were identified to be components of the A-C linkers (Bournonville et al., 2024; Laporte et al., 2024). Within the central core, a helical inner scaffold imparts structural integrity upon the centriole (Le Guennec et al., 2020; Steib et al., 2020), and recruits proteins, including gamma-tubulin, to the lumen of the centriole (Schweizer

et al., 2021). This scaffold is formed in G2-phase of the first cell cycle after centriole birth, is composed of POC5, POC1B, FAM161A, WDR90, and CCDC15 and contacts all three (A-, B-, and C-) tubules of the triplet (Arslanhan et al., 2023; Laporte et al., 2024; Le Guennec et al., 2020; Steib et al., 2020). The distal region of centrioles also has a unique protein composition, including the proteins centrin, CP110, SFI1, CEP97, CEP90, OFD1, and MNR (Kleylein-Sohn et al., 2007; Kumar et al., 2021; Laporte et al., 2022; Laporte et al., 2024; Le Borgne et al., 2022; Spektor et al., 2007). The connections between the compound microtubules and these distal end proteins are not well-understood.

Canonically, centriole formation in cycling cells is “templated,” in which one newly formed procentriole is created at the proximal end of each pre-existing parental centriole in S-phase, resulting in four centrioles within the cell. During the first cycle after their formation, procentrioles acquire post-translational modifications, elongate, recruit the inner scaffold, lose the cartwheel, and undergo centriole-to-centrosome conversion. Additional changes occur during the second cell cycle, including acquisition of the distal and subdistal appendages that are important for ciliogenesis (Sullenberger et al., 2020; Tischer et al., 2021). Under experimental manipulations in which the parental centrioles are ablated, centrioles can also form *de novo* in S-phase. *De novo* centriole formation can result in more than five centrioles per cell and has been shown to be error-prone (Wang et al., 2015), perhaps indicating differences in centriole structure or regulation. The composition and architecture of centrioles made in this manner has not been systematically characterized.

Here, we extend our original work by defining the roles of two additional proteins, TEDC1 and TEDC2, that regulate triplet microtubule formation and stability. These proteins physically interact with TUBD1 and TUBE1 (Breslow et al., 2018; Huttlin et al., 2017; Huttlin et al., 2021). Loss of *Tedc1* or *Tedc2* in 3T3 cells results in a variable distribution of centriole numbers through the cell cycle, and tagged TEDC1 localizes to centrosomes (Breslow et al., 2018). We created *TEDC1*$^{-/-}$ or *TEDC2*$^{-/-}$ mutant cells in the same background as the *TUBD1*$^{-/-}$ and *TUBE1*$^{-/-}$ mutants and found that these cells phenocopy loss of TUBD1 or TUBE1. All four proteins interact in a complex. We find that the compound microtubules are required for recruiting the helical inner scaffold and correctly positioning the proximal end. As part of our analysis, we also determine the composition and architecture of centrioles formed *de novo* and find that these are very similar to those of procentrioles formed by templated centriole duplication. Together, these results indicate that compound microtubules are required for scaffolding substructures within centrioles and maintaining centriole stability through the cell cycle.

Results

Loss of TEDC1 or TEDC2 phenocopies loss of TUBD1 or TUBE1

TEDC1 and TEDC2 have been reported to physically interact with delta-tubulin and epsilon-tubulin, and loss of either *Tedc1* or *Tedc2* in 3T3 cells results in cells with a variable number of centrioles through the cell cycle (Breslow et al., 2018). To further dissect the phenotypes of loss of *TEDC1* or *TEDC2* and directly compare to our original report on delta-tubulin and epsilon-tubulin, we used CRISPR/Cas9 to generate strong loss of function/null mutations in *TEDC1* or

TEDC2 in the same cell type and background genotype (hTERT RPE-1 *TP53*$^{-/-}$, which will be referred to as RPE-1 *p53*$^{-/-}$) as the *TUBD1*$^{-/-}$ (delta-tubulin knockout) and *TUBE1*$^{-/-}$ (epsilon-tubulin knockout) mutant cells (Fig 1 - Supp 1). By immunofluorescence staining for two centriolar proteins, centrin (CETN) and CP110, we observed that *TEDC1*$^{-/-}$ and *TEDC2*$^{-/-}$ mutant cells had similar phenotypes to each other and to *TUBD1*$^{-/-}$ and *TUBE1*$^{-/-}$ mutant cells: in an asynchronously growing culture, about half of the cells had no centrioles, and half had five or more centrioles. These phenotypes were fully rescued by expression of tagged TEDC1 (TEDC1-Halotag-3xFlag) or TEDC2 (TEDC2-V5-APEX2) (Fig 1A, Fig 1 – Supp 1).

Next, we checked whether the centrioles in *TEDC1*$^{-/-}$ and *TEDC2*$^{-/-}$ mutant cells underwent a futile cycle of centriole formation and disintegration. We synchronized cells in each stage of the cell cycle, quantified the number of cells with centrioles, and found that almost all mutant cells lacked centrioles in G0/G1 phase. Centrioles formed in S-phase and disintegrated in M (Fig 1B). The centrioles that were present in mutant cells were immature: all centrioles were positive for the procentriole marker SASS6 and negative for the mature centriole marker CEP164 (Fig 1C, 1D). We conclude that cells lacking TEDC1 or TEDC2 also undergo a futile cycle, similar to cells lacking delta-tubulin or epsilon-tubulin (Fig 1G).

We also examined the centriolar microtubule status of *TEDC1*$^{-/-}$ and *TEDC2*$^{-/-}$ mutant cells by TEM. Similar to cells lacking delta-tubulin or epsilon-tubulin, we found that centrioles in *TEDC1*$^{-/-}$ and *TEDC2*$^{-/-}$ mutant cells lacked compound microtubules and only had singlet microtubules. These centrioles had cartwheels and pinheads, but A-C linkers were not visible (Fig 1E,F, Fig 1 – Supp 2). Together, these results demonstrate that loss of TEDC1 or TEDC2 phenocopies loss of delta-tubulin or epsilon-tubulin, indicating that these proteins likely act together.

TEDC1 and TEDC2 localize to centrosomes

Next, we investigated the localization of TEDC1 and TEDC2 to determine if they may directly act on centrosomes. TEDC1 and TEDC2 are expressed at low levels in cells (Fig 1 – Supp 1), and we could not reproducibly localize the endogenous proteins with antibody staining. Instead, we localized the functional, tagged proteins in our rescue cell lines. We found that the tagged rescue constructs localize to centrosomes, (Fig 2A and 2B) and the antibodies for the tags were specific (Fig 2 - Supp Fig 1E-J). TEDC1 and TEDC2 were enriched at centrosomes in S/G2 and colocalized with SASS6, but not centrin, indicating that TEDC1 and TEDC2 may localize to newly formed procentrioles and/or the proximal ends of parental centrioles.

To analyze TEDC1 and TEDC2 localization at higher resolution, we localized our tagged rescue constructs using three methods: a super-resolution spinning disk confocal microscope with immunofluorescence microscopy (Fig 2 – Supp Fig 1A,B), ultrastructure expansion microscopy (U-ExM, (Gambarotto et al., 2019), Fig 2C, D), and a second expansion microscopy method (Kong et al., 2024, Fig 2 - Supp 1C, D). With all three methods, we observed that both proteins localize to procentrioles and the proximal ends of parental centrioles. At these regions, both proteins overlap with the centriolar microtubules. Together, these results show that TEDC1 and TEDC2 localize to centrosomes and likely directly act upon them.

TEDC1, TEDC2, TUBD1 and TUBE1 form a complex in cells

To determine how TEDC1, TEDC2, TUBD1 and TUBE1 might act together, we first determined whether they are mutually required for their localization at centrosomes. We found that TEDC1 did not localize to centrioles in the absence of TEDC2, TUBD1, or TUBE1 (Figure 3A). Likewise, TEDC2 did not localize to centrioles in the absence of TEDC1, TUBD1, or TUBE1 (Figure 3B). These results indicate that these proteins are mutually required for TEDC1 or TEDC2 localization. Furthermore, overexpression of TEDC1 or TEDC2 did not rescue the centriole phenotypes in any of the other mutants, indicating that TEDC1 and TEDC2 are not downstream effectors of TUBD1 and TUBE1 (Fig 3A and 3B).

TEDC1 and TEDC2 have previously been shown to physically interact with TUBD1 and TUBE1 (Breslow et al., 2018). To further probe the nature of this interaction, we first determined whether any of these proteins may form subcomplexes in cells. We expressed TEDC1-Halotag-3xFlag in each mutant cell line and determined whether immunoprecipitation of tagged TEDC1 could precipitate the other proteins. TEDC1-Halotag-3xFlag rescuing the *TEDC1*$^{-/-}$ mutant could precipitate TEDC2, TUBD1, and TUBE1, indicating that all four proteins physically interact. TEDC1 did not interact with epsilon-tubulin in the absence of delta-tubulin, nor did it interact with delta-tubulin in the absence of TUBE1. In the absence of TEDC2, TEDC1 did not interact with TUBD1 or TUBE1. However, in the absence of TUBD1 or TUBE1, TEDC1 and TEDC2 could still interact with each other (Fig 3C).

We performed the reciprocal experiment, in which we expressed TEDC2-V5-APEX2 in each mutant cell line and determined whether immunoprecipitation of tagged TEDC2 could precipitate the other proteins. We observed similar results as our analysis with TEDC1. TEDC2-V5-APEX2 rescuing the *TEDC2*$^{-/-}$ mutant could precipitate TEDC1, TUBD1, and TUBE1, indicating that all four proteins physically interact. TEDC2 did not interact with either tubulin in the absence of the other. In the absence of TEDC1, TEDC2 did not interact with either tubulin. However, in the absence of TUBD1 or TUBE1, TEDC2 and TEDC1 could still interact (Fig 3D).

Together, these experiments indicate that TEDC1, TEDC2, TUBD1 and TUBE1 physically interact with each other, as previously reported (Breslow et al., 2018; Huttlin et al., 2017; Huttlin et al., 2021). Furthermore, TEDC1 and TEDC2 can form a subcomplex in the absence of either tubulin.

To gain additional insight into the nature of this interaction, we used AlphaFold-Multimer (Evans et al., 2021) to predict the structure of the complex. AlphaFold-Multimer predicted that TUBD1 and TUBE1 would form a heterodimer, similar to the alpha-tubulin/beta-tubulin heterodimer, with TUBD1 at the minus-end of the heterodimer. AlphaFold also predicted that the alpha-helices of TEDC1 and TEDC2 interact with each other, and that TEDC1 and TEDC2 form an interaction surface with TUBD1. These predictions, especially at the interface between TEDC1, TEDC2, and TUBD1, yielded high confidence pLDDT and PAE scores (Fig 3E-G, Fig 3 – Supp 1A). A similar prediction was obtained with the newly released AlphaFold 3 (Abramson et al., 2024)(Fig 3 – Supp 1B). As controls, we used AlphaFold-Multimer to predict whether TEDC1 and TEDC2 might interact with alpha-tubulin and beta-tubulin, and whether similar structures would be

predicted for *Xenopus* TEDC1, TEDC2, TUBD1 and TUBE1. While AlphaFold-Multimer did not predict a high-confidence interaction for TEDC1, TEDC2, alpha- and beta-tubulin (Fig 3 - Supp 1C), it did predict a high-confidence structure for *Xenopus* TEDC1, TEDC2, TUBD1 and TUBE1, similar to that predicted for the human proteins (Fig 3 - Supp 1D).

Our pulldown experiments showed that TEDC1 and TEDC2 can interact in a subcomplex in the absence of TUBD1 or TUBE1, which supports the predicted structural model, in which TEDC1 and TEDC2 are predicted to directly interact with each other without being bridged by either tubulin. Further supporting this model, immunoprecipitation of TEDC2 identifies the other proteins in stoichiometric amounts (Breslow et al., 2018), and we previously showed that TUBD1 and TUBE1 physically interact (Wang et al., 2017). Given the size and shape of the tetrameric complex as predicted by AlphaFold-Multimer, it is possible that these may form a structural component of centrioles. Future work will be necessary to test these possibilities. Together, our experiments indicate that TEDC1, TEDC2, TUBD1 and TUBE1 physically interact in a complex and are recruited together to centrioles.

Loss of TEDC1, TEDC2, TUBD1 or TUBE1 results in centrioles with aberrant ultrastructure

Next, we determined how the loss of these proteins, and the triplet microtubules themselves, affect centriole ultrastructure and protein composition. Because centrioles are constitutively formed *de novo* every cell cycle in our mutant cells, we incorporated two controls in our analysis: procentrioles undergoing normal parental-mediated centriole duplication in control (RPE-1 *p53*$^{-/-}$) cells, and centrioles formed in RPE-1 *p53*$^{-/-}$ cells *de novo* in the first cell cycle after centrinone washout. For each of the 2 control and 4 mutant cell lines, cells were synchronized by mitotic shake off, resulting in coverslips enriched for cells in late S and G2 phases, with a minor population in M phase. Synchronized cells were then expanded using U-ExM and stained for centriolar markers.

We first tested whether the microtubules of mutant centrioles could be modified by acetylation of alpha-tubulin. During centriole formation, acetylation is thought to proceed from the proximal toward the distal end and from the A- to the C-tubules (Sahabandu et al., 2019). We found that antibodies against acetylated alpha-tubulin stained mutant centrioles well (Fig 4B), indicating that centrioles with only singlet A-tubules can be acetylated.

We next tested whether mutant centrioles were capable of elongating during the cell cycle. In our expansion gels of cells enriched in late S and G2 phases, we used PCNA to mark S-phase cells and co-stained with acetylated tubulin to mark centrioles. Similar to a recently published report, we also found a range of centriole lengths in S- and G2-phases (Laporte et al., 2024). In S-phase, centrioles were short in all conditions. In G2-phase, centrioles elongated in all conditions, and mutant centrioles reached approximately similar lengths as control centrioles (Fig 4A). By contrast, mutant centriole widths did not increase and centrioles remained narrow, as we previously reported (Fig 4 – Supp 5 and Wang et al., 2017). These results indicate that centrioles with singlet microtubules can elongate to the same overall length as control centrioles

in G2 phase. Consistent with this hypothesis, CEP120, a protein involved in regulating centriole length (Comartin et al., 2013; Lin et al., 2013b; Mahjoub et al., 2010), was present and properly localized within mutant centrioles (Fig 4 - Supp 1D).

The compound microtubules of centrioles are heavily post-translationally modified, and recent studies have indicated that each tubule may acquire different modifications (Guichard et al., 2023). We checked glutamylation, a post-translational modification thought to be restricted to the outer surface of centrioles (Guichard et al., 2023). Within *Chlamydomonas* centrioles, glutamylation is differentially distributed between each tubule: on the C-tubule at the distal end, on all 3 tubules in the central core, and on the A-tubule at the proximal end (Hamel et al., 2017). In human centrioles, polyglutamylation is enriched in the proximal and central regions, and is absent in the distal region (Gambarotto et al., 2019; Mahecic et al., 2020; Sullenberger et al., 2020). We used two antibodies to detect glutamylation: the GT335 antibody, which recognizes the glutamylation branch and thus detects all polyglutamylation, and the polyE antibody, which recognizes long polyglutamate side chains with at least 2 or 3 glutamate residues (Kann et al., 2003; Van Dijk et al., 2007). We found that mutant and control centrioles could be stained by GT335 (Fig 4C), indicating that mutant centrioles are at least mono-glutamylated. However, the polyE antibody did not label control procentrioles or *de novo* centrioles in the first cell cycle after their formation, making this antibody uninformative for our mutants (Fig 4D). These results show that centrioles with just singlet microtubules (A-tubules) can be mono-glutamylated. Moreover, similar to previous reports (Sullenberger et al., 2020), our results suggest that centriole glutamylation is a multi-step process, in which long glutamate side chains are added later during centriole maturation.

We previously demonstrated that *TUBD1*$^{-/-}$ and *TUBE1*$^{-/-}$ mutant centrioles fail to recruit the distal centriole protein POC5 (Wang et al., 2017). Using expansion microscopy, we found that *TEDC1*$^{-/-}$ and *TEDC2*$^{-/-}$ mutant centrioles also failed to recruit POC5 (Fig 4Ei). Since our original work was published, POC5 was shown to be a component of the helical inner scaffold within the central core. These results indicate that the helical inner scaffold is not properly formed in centrioles with singlet microtubules. To test the mechanisms underlying loss of POC5, we next tested whether mutant centrioles recruit WDR90, which has been proposed to localize to the inner junction between the A- and B-tubules and function in recruiting the inner scaffold (Steib et al., 2020). We found that WDR90 was not recruited to mutant centrioles, in contrast to control centrioles, in which it is recruited in G2-phase (Fig 4Eii). From these results, it is likely that mutant centrioles with singlet microtubules fail to build or stabilize the inner junction between the A- and B-tubules. In the absence of the inner junction and junctional protein WDR90, centrioles with singlet microtubules cannot form the inner scaffold. As also previously reported (Laporte et al., 2024), we failed to detect gamma-tubulin within the lumen of control or *de novo*-formed centrioles in S or G2-phase (Fig 4-Supp1E) and thus were unable to test whether gamma-tubulin, which is recruited to the lumen of centrioles by the inner scaffold, was mislocalized in mutant centrioles.

Next, we tested whether the centriole proximal end might be properly formed in mutant centrioles. We found that the centriolar cartwheel protein, SASS6, was present within the lumen

298 of control and mutant centrioles in S-phase. In control centrioles in G2-phase, SASS6 was
299 restricted to just the proximal end. Surprisingly, SASS6 was elongated in all G2-phase mutant
300 centrioles (Fig 4F, Fig 4 – Supp 4). We observed a similar phenotype with multiple other
301 proximal-end proteins: CEP135, STIL, CPAP, and CEP44 (Fig 4G-I, Fig 4 - Supp 1, Fig 4 –
302 Supp 3), indicating that the entire proximal end is elongated in mutant centrioles. The extended
303 localization of proximal end proteins was not due to increased protein expression in mutant cells
304 (Fig 4 - Supp 2). We conclude that loss of TEDC1, TEDC2, TUBD1, or TUBE1 results in
305 elongated proximal end domains within mutant centrioles.
306
307 Elongation of the proximal end of centrioles may also indicate an overall defect in centriole
308 polarity. To test this hypothesis, we next determined whether these mutant centrioles might
309 properly recruit proteins to their distal ends. We found that CETN2 and CP110, two proteins of
310 the distal centriole, were localized to mutant centrioles and clearly marked one end of the
311 centriole barrel in both S-phase and G2-phase (Fig 4 - Supp 1B, 1C). We conclude that
312 proximal-to-distal centriole polarity was unaffected in mutant centrioles, and proximal end
313 elongation did not affect the recruitment of proteins to the centriole distal end. Together, these
314 results indicate that centrioles lacking compound microtubules are unable to properly regulate
315 the length of the proximal end.
316
317 **Mutant centrioles elongate further in mitosis before fragmenting**
318
319 Centrioles lacking triplet microtubules undergo a futile cycle of formation and disassembly, but
320 the mechanisms underlying disassembly are not well-understood. We first tested whether
321 centriole loss in mutant centrioles may be due to loss of CEP295. CEP295 promotes centriole-
322 to-centrosome conversion, a process in which pericentriolar material is recruited to newly-
323 formed procentrioles. Cells lacking CEP295 form centrioles that disintegrate during the cell
324 cycle due to a failure to undergo centriole-to-centrosome conversion (Izquierdo et al., 2014).
325 Using U-ExM, we found that CEP295 was present and normally localized within mutant
326 centrioles in both S- and G2-phases (Fig 4 - Supp 1F). We conclude that centriole loss in our
327 mutants is unlikely to be due to loss of CEP295 localization, and therefore that TEDC1, TEDC2,
328 TUBD1 and TUBE1 are likely part of a different pathway required for centriole stability through
329 the cell cycle.
330
331 Next, we used U-ExM to visualize centriole loss during mitosis. We stained for the centriole wall
332 (GT335), the centriole proximal end (SASS6) and the centriole distal end (CP110). In control
333 cells, in which centrioles formed *de novo* after centrinone washout, multiple centrioles could be
334 seen throughout mitosis, and SASS6 was lost from centrioles in anaphase-stage cells (Fig
335 5A,B). By contrast, in prometaphase stage *TUBD1*$^{-/-}$ or *TUBE1*$^{-/-}$ cells, we found that centrioles
336 had a unique appearance: they were longer than normal, with an elongated proximal end
337 marked by SASS6, and a CP110-positive cap. These two ends were connected by weak monoE
338 staining (Fig 5C, 5E). This phenotype is identical to our observations of centrioles in a
339 prometaphase *TUBE1*$^{-/-}$ cell by TEM in our previous publication (Wang et al., 2017, Fig 2B).
340 After metaphase, centrioles in mutant cells were either completely absent, or had a fragmented
341 appearance (Fig 5D, 5F), with aggregates of staining that did not resemble true centrioles. We

342 conclude that in our mutant cells, centrioles elongate in early mitosis to form an aberrant
343 intermediate structure, followed by fragmentation in late mitosis.
344

345 Discussion

346
347 Here, we extend our previous study on delta-tubulin (TUBD1), epsilon-tubulin (TUBE1) and the
348 centriolar triplet microtubules. Previously, we showed that loss of either of these proteins from
349 mammalian cultured cell lines results in the same phenotype: loss of the triplet microtubules and
350 a futile cycle of centriole formation and disintegration (Wang et al., 2017). Here, we add two new
351 proteins to this pathway: TEDC1 and TEDC2, which were originally identified by their
352 association with TUBD1 and TUBE1 (Breslow et al., 2018; Huttlin et al., 2017; Huttlin et al.,
353 2021). Loss of TEDC1 or TEDC2 phenocopies the loss of TUBD1 or TUBE1: aberrant centrioles
354 are formed that lack triplet microtubules and disintegrate during passage through mitosis.
355 TEDC1 and TEDC2 localize to centrioles, indicating that they have a direct role in forming or
356 maintaining centriole structure, and their localization depends on each of the other three
357 proteins within the complex. All four proteins physically interact with each other. Using our
358 mutant cell lines, we interrogated whether any of these proteins can form subcomplexes within
359 cells. We found that TEDC1 and TEDC2 can interact with each other independently of the
360 tubulins, supporting a predicted AlphaFold-Multimer model. Together, these results indicate that
361 these four proteins act together in a complex at centrosomes to form or stabilize the compound
362 microtubules.
363
364 While the molecular mechanisms underlying the function of this complex are unknown, an
365 attractive model is that the tetrameric complex forms a structural component of centrioles. Our
366 AlphaFold models indicate that such a structure would be approximately 13 nm in length and 6
367 nm in width. Within procentrioles and the proximal region of the parental centriole, it is possible
368 that these four proteins help form the A-C linker, the pinhead, or the triplet base. Recently,
369 components of the A-C linker have been identified (Bournonville et al., 2024; Laporte et al.,
370 2024), and three of the proteins in our complex (TEDC2, TUBD1, and TUBE1) had shared co-
371 dependencies with A-C linker components using DepMap (Bournonville et al., 2024). The A-C
372 linker is lost from our mutant centrioles, but it is not clear whether this is because these proteins
373 have a direct role in forming A-C linkers or whether this reflects an indirect role of the triplet
374 microtubules in stabilizing A-C linkers. We note that it is also possible that only some proteins of
375 the complex, such as delta-tubulin and epsilon-tubulin, form structural components of centrioles,
376 or that the complex may interact transiently with centrioles. Future experiments will reveal the
377 mechanisms by which these proteins act.
378
379 Using ultrastructure expansion microscopy, we find that mutant centrioles with singlet
380 microtubules exhibit additional major architectural defects, including absence of the inner
381 scaffold and elongation of the proximal end. We propose that the absence of the inner scaffold
382 arises from the loss of the B- and C-tubules within centrioles, which may serve to anchor
383 WDR90 and/or other proteins of the inner scaffold. WDR90 has been proposed to localize to the
384 inner junction between the A- and B-tubules and is required for recruiting other inner scaffold
385 components (Le Guennec et al., 2020; Steib et al., 2020). We find that mutant centrioles with

386 singlet microtubules fail to localize WDR90, and thus speculate that the B-tubule is required to
387 recruit or stabilize WDR90 at the inner junction. In addition, by cryo-electron tomography, the
388 inner scaffold makes connections to all three (A-, B-, and C-) tubules. Though the identities of all
389 the proteins that form these connections have not been determined, it is possible that mutant
390 centrioles with only A-tubules also fail to provide anchoring sites for the other proteins within the
391 inner scaffold. Together, these results demonstrate that the compound microtubules of
392 centrioles are required for proper formation of the inner helical scaffold of the central core.
393
394 Mutant centrioles with singlet microtubules have an elongated proximal end that extends the
395 entire length of the centriole, as marked by multiple proximal end markers (SASS6, CEP135,
396 STIL, CPAP, CEP44). These results are also supported by our previous observations that by
397 TEM, the lumen of *TUBD1*$^{-/-}$ and *TUBE1*$^{-/-}$ mutant centrioles are filled with electron-dense
398 material (Wang et al., 2017). Little is known about the molecular mechanisms that regulate
399 proximal end length, though centrioles from the symbiotic flagellate *Trichonympha* bear an
400 elongated proximal region with extended cartwheel, and the doublet and singlet-bearing
401 centrioles from *Drosophila* and *C. elegans* have cartwheels that extend the entire length of the
402 centriole (González et al., 1998; Guichard and Gönczy, 2016; Guichard et al., 2012; Pelletier et
403 al., 2006; Woglar et al., 2022). It is possible that the triplet microtubules, the inner scaffold,
404 and/or the TUBD1/TUBE1/TEDC1/TEDC2 protein complex might act to limit the length of the
405 proximal end. Recently, loss of the inner scaffold protein POC1A has been shown to result in
406 centrioles with extended regions of some proximal proteins, including CEP44, CEP135, and
407 CEP295, indicating that the inner scaffold regulates the extent of these proteins (Sala et al.,
408 2024). Interestingly, unlike our mutant centrioles which have singlet microtubules, *POC1A*$^{-/-}$
409 mutant centrioles can form triplet microtubules and do not have extended SASS6 staining (Sala
410 et al., 2024). This suggests that the height of the cartwheel may be regulated by the triplet
411 microtubules. The cartwheel and centriolar microtubules have been proposed to assemble
412 interdependently to impart ninefold symmetry upon the centriole (Hilbert et al., 2016), and it is
413 possible that interdependent assembly also regulates the height of the cartwheel.
414
415 Many aspects of centriole architecture, including formation of the distal tip, centriole length
416 regulation prior to mitosis, acquisition of post-translational modifications, establishment of
417 proximal-distal polarity, and recruitment of proteins required for centriole-to-centrosome
418 conversion, are unaffected in mutant centrioles. These results indicate that the proteins that
419 regulate these processes can act upon the A-tubule independently of the B- and C-tubules.
420
421 Here, we also extend our previous observations of centriole loss in mutant centrioles. In most
422 cell types, centrioles are inherited by daughter cells during each mitosis. Centriole loss is not
423 unique to centrioles lacking compound microtubules: mammalian cells engineered to lack
424 CEP295 also form centrioles that are lost through the cell cycle, due to an inability to undergo
425 centriole to centrosome conversion (Izquierdo et al., 2014). Similarly, in *Drosophila* oocytes,
426 down-regulation of Polo kinase and pericentriolar material triggers centriole elimination
427 (Pimenta-Marques et al., 2016). We find that CEP295 is properly localized in mutant centrioles
428 with singlet microtubules, indicating that centriole loss in this context may be independent of
429 centriole to centrosome conversion and pericentriolar material recruitment. Using expansion

microscopy, we find that centriole loss is correlated with loss of the SASS6 cartwheel in mitosis. In this regard, mutant centrioles with singlet microtubules resemble centriole loss within *C. elegans* oocytes, in which an analogous structure to the cartwheel named the central tube is lost prior to centriole widening and subsequent loss of the centriolar microtubules (Pierron et al., 2023). In addition, centriole loss in our mutant cells occurs through a stereotyped progression of architectural changes in mitosis, starting with centriole over elongation in prometaphase and culminating with centriole fragmentation and loss. Prolonged mitotic arrest has been reported to result in centriole over elongation through Plk1 activity (Kong et al., 2020), and it is possible that a lengthened mitosis, as observed in these mutant cells and cells lacking centrioles (Farrell et al., 2024; Wang et al., 2017), may also result in over elongation of mutant centrioles with just A-tubules. In addition, we note that CPAP has an expanded domain in mutant centrioles compared to controls (Fig 4, (Vásquez-Limeta et al., 2022). CPAP is involved in slow processive microtubule growth (Sharma et al., 2016) and its loss results in centriole fragmentation (Vásquez-Limeta et al., 2022), and it is possible that CPAP mislocalization may also contribute to over elongation of these mutant centrioles. Future work will determine the molecular mechanisms by which mutant centrioles lacking triplet microtubules are disassembled through the cell cycle.

Finally, we note that mutant human centrioles lacking compound microtubules bear similarities to the centrioles of *Drosophila* and *C. elegans* embryos, which have evolved to lack triplet microtubules and have cartwheels extending the entire length of the centriole (González et al., 1998; Pelletier et al., 2006; Woglar et al., 2022). Embryonic centrioles in both species are shorter than that of other organisms, and helical inner scaffolds have not been reported. In both species, these diminished centrioles participate in mitosis, can duplicate their centrioles, and serve as basal bodies for sensory cilia. We speculate that centrioles with triplet microtubules and the proteins they anchor, including the inner scaffold, may be required for centriole function in organisms with motile cilia, perhaps to help stabilize the basal body against ciliary movement. Such activity has been described for *Tetrahymena* basal bodies, and mutating an inner scaffold protein, Poc1, results in abnormal bending within basal bodies (Junker et al., 2022). Further supporting this hypothesis, *Drosophila* spermatocytes, one of the few cells within this species with motile cilia, have basal bodies with triplet microtubules (González et al., 1998). We note that these spermatocytes likely form triplet microtubules in an alternative manner, as *Drosophila* lacks delta-tubulin or epsilon-tubulin.

In conclusion, this work, along with our previously published study, identifies proteins required for the formation or maintenance of the centriolar triplet microtubules and maps the requirements of these proteins and the triplets in centriole architecture. Together, these results pave the way for deeper molecular understanding of the mechanisms by which the triplet microtubules are formed and maintained reproducibly within cells to form robust centrioles and cilia.

Figure legends

Figure 1. Loss of TEDC1 or TEDC2 phenocopies loss of delta-tubulin or epsilon-tubulin **(A)** Immunofluorescence staining of control (RPE1 *TP53*$^{-/-}$), *TEDC1*$^{-/-}$ (RPE1 *TP53*$^{-/-}$; *TEDC1*$^{-/-}$), TEDC1 Rescued (RPE1 *TP53*$^{-/-}$; *TEDC1*$^{-/-}$; TEDC1-Halotag-3xflag), *TEDC2*$^{-/-}$ (RPE1 *TP53*$^{-/-}$; *TEDC2*$^{-/-}$), TEDC2 Rescued (RPE1 *TP53*$^{-/-}$; *TEDC2*$^{-/-}$; Tedc2-V5-APEX2) cells. Top row: G1 stage cells with 2 centrioles. Bottom row: S/G2 stage cells with 4 centrioles. Blue: DAPI; Yellow: Centrin (CETN); Magenta: CP110. Images are maximum projections of confocal stacks. Scale bar: 5 um **(B)** Centriole number counts of the indicated cell lines. Cells were either asynchronous, serum-starved for G0/G1, stained for PCNA for S-phase, synchronized with RO-3306 for G2/M, or mitotic figures were identified by DAPI staining. Each condition was performed in triplicate, with n=100 cells scored for each. **(C)** Percent of all centrioles (parental, pro, and *de novo* centrioles) in indicated cell types positive for SASS6 staining. Each condition was performed in triplicate, with 200 cells scored for each. (D) Percent of all centrioles (parental, pro, and *de novo* centrioles) in indicated cell types positive for CEP164 staining. Each condition was performed in triplicate, with 100 cells scored for each. **(E)** TEM cross-section of a centriole in a G2-phase *TEDC1*$^{-/-}$ cell. Scale bar: 100 nm **(F)** TEM cross-section of a centriole in a G2-phase *TEDC2*$^{-/-}$ cell. Scale bar: 100 nm **(G)** Schematic of centriole formation and loss in control and *TEDC1*$^{-/-}$ or *TEDC2*$^{-/-}$ cells.

Figure 1 - Supplementary Figure 1. Genotyping of *TEDC1*$^{-/-}$ and *TEDC2*$^{-/-}$ mutant cell lines **(A)** Gene structure of the TEDC1 locus in parental *TP53*$^{-/-}$ cells and the *TEDC1*$^{-/-}$ mutant. Green boxes: exons; blue lines: introns; red triangles: sgRNA binding sites; black arrow: translation start site. The *TEDC1*$^{-/-}$ mutant (clone 2F4) is a compound heterozygote bearing a deletion of 227 bp on one allele and a deletion of 329 bp on the other allele. In both alleles, the ATG start site is deleted and the next ATG is not in-frame. **(B)** Gene structure of the TEDC2 locus in parental *TP53*$^{-/-}$ cells and the *TEDC2*$^{-/-}$ mutant. Green boxes: exons; blue lines: introns; red triangles: sgRNA binding sites; black arrow: translation start site. The *TEDC2*$^{-/-}$ mutant (clone F5) is a compound heterozygote bearing a deletion of 19 bp on one allele flanking the ATG start site. On the other allele, there is an insertion of 306 bp corresponding to a fusion between TEDC2 and the hCLHC1 gene. In both alleles, the ATG start site is deleted, the next ATG is not in-frame, and no additional ATG start sites are found. **(C)** Genotyping PCR of the Tedc1 locus in parental *TP53*$^{-/-}$ cells, the *TEDC1*$^{-/-}$ mutant, and TEDC1 Rescued (RPE1 *TP53*$^{-/-}$; *TEDC1*$^{-/-}$; TEDC1-Halotag-3xflag) cells. Top: PCR for TEDC1. Bottom: PCR for Halotag. **(D)** Genotyping PCR of the TEDC2 locus in parental *TP53*$^{-/-}$ cells, the *TEDC1*$^{-/-}$ mutant, and TEDC2 Rescued (RPE1 *TP53*$^{-/-}$; *TEDC2*$^{-/-}$; TEDC2-V5-APEX2) cells. Top: PCR for TEDC2. Bottom: PCR for APEX2. **(E)** Western blot of TEDC1 protein levels in parental *TP53*$^{-/-}$ cells, the *TEDC1*$^{-/-}$ mutant, and TEDC1 Rescued (RPE1 *TP53*$^{-/-}$; *TEDC1*$^{-/-}$; TEDC1-Halotag-3xflag) cells. Total protein stain is used as a loading control. TEDC1-Halotag-3xFlag is overexpressed 73-fold above endogenous levels (average of 3 independent experiments). Asterisks mark non-specific bands. **(F)** Western blot of TEDC2 protein levels in parental *TP53*$^{-/-}$ cells, the *TEDC2*$^{-/-}$ mutant, and TEDC2 Rescued (RPE1 *TP53*$^{-/-}$; *TEDC2*$^{-/-}$; TEDC2-V5-APEX2) cells. Total protein stain is used as a loading control. TEDC2-V5-APEX2 is overexpressed 26-fold above endogenous levels (average of 3 independent experiments). Asterisks mark non-specific bands.

514
515 **Figure 1 - Supplementary Figure 2. Symmetrization of *TEDC1*$^{-/-}$ and *TEDC2*$^{-/-}$ mutant**
516 **centrioles**
517 Original (left) and symmetrized (right) images of TEM images of *TEDC1*$^{-/-}$ and *TEDC2*$^{-/-}$
518 centrioles. The first image is the same as that in Fig 1E, the last image is the same as that in Fig
519 1F. The middle image is an additional centriole from the *TEDC1*$^{-/-}$ mutant cells.
520
521 **Figure 2. Tedc1 and Tedc2 localize to centrioles**
522 **(A)** Immunofluorescence staining of Tedc1 rescue cell lines expressing TEDC1-Halotag-3xFlag
523 in G1, S/G2, and M. Images are maximum projections of confocal stacks. Blue: DAPI; Cyan:
524 Centrin; Magenta: TEDC1-Halotag-3xFlag (localized with anti-Flag antibody); Yellow: SASS6.
525 Scale bar: 5 um. **(B)** Immunofluorescence staining of Tedc2 rescue cell lines expressing
526 TEDC2-V5-APEX2 in G1, S/G2, and M. Images are maximum projections of confocal stacks.
527 Blue: DAPI; Cyan: Centrin (localized with anti-GFP antibody recognizing GFP-centrin);
528 Magenta: TEDC2-V5-APEX2 (localized with anti-V5 antibody); Yellow: SASS6. Scale bar: 5 um.
529 **(C)** U-ExM of Tedc1 rescue cell lines expressing TEDC1-Halotag-3xFlag, arranged by
530 procentriole length. Cyan: Acetylated tubulin; Magenta: TEDC1-Halotag-3xFlag (localized with
531 anti-Flag antibody). Confocal image stacks were deconvolved using Microvolution; single plane
532 images shown. Scale bar: 1 um. **(D)** U-ExM of Tedc2 rescue cell lines expressing TEDC2-V5-
533 APEX2, arranged by procentriole length. Cyan: Acetylated tubulin; Magenta: TEDC2-V5-APEX2
534 (localized with anti-V5 antibody). Confocal image stacks were acquired with a Yokogawa CSU-
535 W1 spinning disk microscope and deconvolved using Microvolution; single plane images shown.
536 Scale bar: 1 um.
537
538 **Figure 2 - Supplementary Figure 1. Extended localization analyses of TEDC1 and TEDC2**
539 **(A)** Immunofluorescence staining of a TEDC1 rescue cell in G2 phase expressing TEDC1-
540 Halotag-3xFlag, super-resolution image using SoRA disk and 2.8x relay. Maximum projection.
541 Cyan: Centrin (CETN); Magenta: TEDC1-Halotag-3xFlag (localized with anti Flag antibody);
542 Yellow: SASS6. Scale bar: 0.5 um **(B)** Immunofluorescence staining of a TEDC2 rescue cell in
543 G2 phase expressing TEDC2-V5-APEX2, super-resolution image using SoRA disk and 2.8x
544 relay. Maximum projection. Cyan: Centrin (CETN); Magenta: TEDC2-V5-APEX2 (localized with
545 anti V5 antibody); Yellow: SASS6. Scale bar: 0.5 um **(C)** Expansion microscopy image of
546 TEDC1 rescue cells expressing TEDC1-Halotag-3xFlag. Expansion gel was made as described
547 in (Kong et al., 2024). The procentriole is oriented vertically. Cyan: CEP44; Magenta: TEDC1-
548 Halotag-3xFlag (localized with anti-Flag antibody). Deconvolved using Microvolution; maximum
549 projection. Scale bar: 1 um. **(D)** Expansion microscopy image of TEDC2 rescue cells expressing
550 TEDC2-V5-APEX2. Expansion gel was made as described in (Kong et al., 2024). The
551 procentriole is oriented vertically. Cyan: CEP44; Magenta: TEDC2-V5-APEX2 (localized with
552 anti-V5 antibody). Deconvolved using Microvolution; maximum projection of confocal stacks.
553 Scale bar: 1 um. **(E)** Immunofluorescence staining of *TP53*$^{-/-}$ cells expressing Halotag-Flag -
554 negative control for Fig 2A. Images are maximum projections of confocal stacks and were
555 acquired with the same exposure settings as in Fig 2A. Blue: DAPI; Cyan: Centrin; Magenta:
556 Flag; Yellow: SASS6. Scale bar: 5 um. **(F)** Immunofluorescence staining of *TP53*$^{-/-}$ cells
557 expressing V5-APEX2 - negative control for Fig 2B. Images are maximum projections of

558 confocal stacks and were acquired with the same exposure settings as in Fig 2B. Blue: DAPI;
559 Cyan: Centrin (localized with anti-GFP antibody recognizing GFP-centrin); Magenta: V5; Yellow:
560 SASS6. Scale bar: 5 um. **(G)** U-ExM of *TP53*$^{-/-}$ cells expressing Halotag-Flag - negative control
561 for Fig 2C. Cyan: Acetylated tubulin; Magenta: Flag. Confocal image stacks were deconvolved
562 using Microvolution; single plane images shown. Images were acquired using the same
563 parameters as Fig 2C. Scale bar: 1 um. **(H)** U-ExM of *TP53*$^{-/-}$ cells expressing V5-APEX2 -
564 negative control for Fig 2D. Cyan: Acetylated tubulin; Magenta: V5. Confocal image stacks were
565 deconvolved using Microvolution; single plane images shown. Images were acquired using the
566 same parameters as Fig 2D. Scale bar: 1 um. **(I)** Expansion microscopy image of *TP53*$^{-/-}$ cells
567 stained with Flag antibody, negative control for Fig 2 – Supp 1C. Cyan: CEP44; Magenta: Flag.
568 Confocal image stacks were deconvolved using Microvolution; image is a maximum projection
569 of confocal stack. Scale bar: 1 um. **(J)** Expansion microscopy image of *TP53*$^{-/-}$ stained with V5
570 antibody, negative control for Fig 2 – Supp 1D. Cyan: CEP44; Magenta: V5. Confocal image
571 stacks were deconvolved using Microvolution; image is a maximum projection of confocal stack.
572 Scale bar: 1 um.
573
574 **Figure 3. TEDC1, TEDC2, TUBD1, TUBE1 form a complex in cells**
575 **(A) Centrosomal TEDC1 localization depends on TEDC2, TUBD1, TUBE1.**
576 Immunofluorescence staining of cells expressing TEDC1-Halotag-3xflag. Control cell is *TEDC1*$^{-}$
577 $^{/-}$ mutant cells rescued with TEDC1-Halotag-3xflag. Images are maximum projections of
578 confocal stacks. Blue: DAPI; Cyan: SASS6; Magenta: TEDC1-Halotag-3xFlag (localized with
579 anti-Flag antibody). Scale bar: 5 um. **(B) Centrosomal TEDC2 localization depends on**
580 **TEDC1, TUBD1, TUBE1.** Immunofluorescence staining of cells expressing TEDC2-V5-APEX2.
581 Control cell is TEDC2 mutant cells rescued with TEDC2-V5-APEX2. Images are maximum
582 projections of confocal stacks. Blue: DAPI; Cyan: SASS6; Magenta: TEDC2-V5-APEX2
583 (localized with anti-V5 antibody). Scale bar: 5 um. **(C) TEDC1 pulls down TEDC2 in the**
584 **absence of delta or epsilon-tubulin.** Western blot of input and pulldown of Halotag-Flag or
585 TEDC2-Halotag-Flag in the indicated cell lines. IB: indicates the antibody used for
586 immunoblotting. The proteins and their positions are labeled on the right. Asterisks mark non-
587 specific bands. **(D) TEDC2 pulls down TEDC1 in the absence of delta or epsilon-tubulin.**
588 Western blot of input and pulldown of TUBA1B-V5-APEX2 or TEDC2-V5-APEX2 in the
589 indicated cell lines. IB: indicates the antibody used for immunoblotting. The proteins and their
590 positions are labeled on the right. Asterisks mark non-specific bands. **(E)** AlphaFold-Multimer
591 prediction of the complex **(F)** AlphaFold-Multimer prediction colored according to pLDDT. Very
592 high: pLDDT > 90. High: 90 > pLDDT > 70. Low: 70 > pLDDT > 50. Very low: pLDDT <50 **(G)**
593 Predicted align error of the AlphaFold Multimer prediction. Expected position error (Angstroms)
594 is graphed.
595

596 **Fig 3 - Supplementary Figure 1. AlphaFold-Multimer and AlphaFold3 predictions**
597 **(Ai)** Rotated view of the AlphaFold-Multimer prediction from Fig 3E (120 degrees around the y-
598 axis) **(Aii)** Rotated view colored according to pLDDT. Very high: pLDDT > 90. High: 90 >
599 pLDDT > 70. Low: 70 > pLDDT > 50. Very low: pLDDT <50 **(Aiii)** Rotated view of the
600 AlphaFold-Multimer prediction from Fig 3E (240 degrees around the y-axis) **(Aiv)** Rotated view
601 colored according to pLDDT. Very high: pLDDT > 90. High: 90 > pLDDT > 70. Low: 70 >
602 pLDDT > 50. Very low: pLDDT <50 **(Bi)** AlphaFold3 prediction of the complex **(Bii)** AlphaFold3
603 prediction colored according to pLDDT. Very high: pLDDT > 90. High: 90 > pLDDT > 70. Low:
604 70 > pLDDT > 50. Very low: pLDDT <50 **(Biii)** Predicted align error of the AlphaFold3
605 prediction. Expected position error (Angstroms) is graphed). **(Biv)** Structural alignment between
606 the AlphaFold3 prediction (magenta) and the AlphaFold-Multimer prediction (cyan). Using
607 ChimeraX v1.7.1 Matchmaker, the RMSD between 450 pruned atom pairs is 0.538 angstroms
608 (across all 475 pairs: 0.979). **(Ci)** AlphaFold-Multimer prediction of TEDC1, TEDC2, TUBA1A,
609 TUBB **(Cii)** AlphaFold-Multimer prediction from Ci) colored according to pLDDT. Very high:
610 pLDDT > 90. High: 90 > pLDDT > 70. Low: 70 > pLDDT > 50. Very low: pLDDT <50 **(Ciii)**
611 Predicted align error of the AlphaFold-Multimer prediction from Ci). Expected position error
612 (Angstroms) is graphed. **(Di)** AlphaFold Multimer prediction of *Xenopus* TEDC1, TEDC2,
613 TUBD1, TUBE1 **(Dii)** AlphaFold-Multimer prediction from Di) colored according to pLDDT. Very
614 high: pLDDT > 90. High: 90 > pLDDT > 70. Low: 70 > pLDDT > 50. Very low: pLDDT <50 **(Diii)**
615 Predicted align error of the AlphaFold-Multimer prediction from Di). Expected position error
616 (Angstroms) is graphed.
617
618 **Figure 4. Mutant centrioles elongate in G2 but fail to recruit central core proteins and**
619 **have an expanded proximal region**
620 **(A)** Lengths of expanded centrioles from cells of the indicated cell cycle stages. Lengths were
621 adjusted for the gel expansion factors. Cells were synchronized in S/G2/M and S-phase cells
622 were marked with PCNA. For each genotype, the differences between S and G2 phase centriole
623 lengths are statistically significant (<0.0001, Welch's t-test). **(B)** U-ExM images of centrioles
624 stained for alpha-tubulin and acetylated tubulin. **(C)** U-ExM of centrioles in S or G2 phase
625 stained with monoE (GT335) antibody. **(D)** U-ExM of control centrioles in S or G2 phase stained
626 with acetylated tubulin and polyE antibodies **(E) i)** U-ExM of centrioles in G2 phase stained with
627 acetylated tubulin (cyan) and POC5 (magenta) antibodies. POC5 is present in the central core
628 of control procentrioles and *de novo* centrioles and absent from mutants. **(ii)** U-ExM of
629 centrioles in G2 phase stained with acetylated tubulin (cyan) and WDR90 (magenta) antibodies.
630 WDR90 is present in the central core of control procentrioles and *de novo* centrioles, and
631 absent from mutants. **(F, G, H, I)** U-ExM of centrioles in S and G2 phase stained for alpha
632 tubulin (cyan) or acetylated tubulin (Ac.Tub, cyan) and the following antibodies in magenta: F)
633 SASS6, G) CEP135, H) STIL, I) CPAP. In control centrioles, these proteins are limited to the
634 proximal end. In mutant centrioles, these proteins are present at the proximal end in S phase
635 centrioles and elongate throughout the entire centriole in G2 phase. Images were acquired with
636 a Yokogawa CSU-W1 SoRA with 2.8x relay and deconvolved with 10 iterations using
637 Microvolution. Scale bars: 1 um.
638

Figure 4 - Supplementary figure 1 - Extended analyses of mutant centriole architecture and U-ExM gel expansion factor

(A, B, C, D, E, F) U-ExM of centrioles in S and G2 phase stained for acetylated tubulin (cyan) and the following proteins in magenta: A) CEP44, B) CETN2, C) CP110, D) CEP120, E) gamma-tubulin, F) CEP295. Scale bars = 1 um. Images were acquired with a Yokogawa CSU-W1 SoRA with 2.8x relay and deconvolved with 10 iterations using Microvolution.

(G) Measurements of the widths of parental centrioles from each experiment as a readout of expansion factor, including the cell cycle analyses in Fig 4A and Fig 4B. Centriole widths were a mean of 1.0 um, corresponding to a four-fold expansion factor.

Figure 4 - Supplementary figure 2 - Total protein levels of centrosomal proteins are unchanged in mutant cells

(A) Western blot of control (RPE1 *TP53*$^{-/-}$), *TEDC1*$^{-/-}$, *TEDC2*$^{-/-}$, *TUBD1*$^{-/-}$, *TUBE1*$^{-/-}$, *SASS6*$^{-/-}$ cell lysates, immunoblotted for SASS6. Total protein stain (Revert) serves as a loading control. **(B)** Western blot of control (RPE1 *TP53*$^{-/-}$), *TEDC1*$^{-/-}$, *TEDC2*$^{-/-}$, *TUBD1*$^{-/-}$, *TUBE1*$^{-/-}$ cell lysates, immunoblotted for STIL. Total protein stain (Revert) serves as a loading control. **(C)** Western blot of control (RPE1 *TP53*$^{-/-}$), *TEDC1*$^{-/-}$, *TEDC2*$^{-/-}$, *TUBD1*$^{-/-}$, *TUBE1*$^{-/-}$ cell lysates, immunoblotted for CPAP. Total protein stain (Revert) serves as a loading control. **(D)** Western blot of control (RPE1 *TP53*$^{-/-}$), *TEDC1*$^{-/-}$, *TEDC2*$^{-/-}$, *TUBD1*$^{-/-}$, *TUBE1*$^{-/-}$ cell lysates, immunoblotted for POC5. Total protein stain (Revert) serves as a loading control.

Figure 4 - Supplementary figure 3 – Quantification of CEP135 centriolar localization through S and G2 phase

Mutant centrioles have over-elongated CEP135. A) control procentrioles, n=29 centrioles; B) *de novo* centrioles, n=42 centrioles; C) *TUBD1*$^{-/-}$, n=32 centrioles; D) *TUBE1*$^{-/-}$, n=30 centrioles; E) *TEDC1*$^{-/-}$, n=23 centrioles; F) *TEDC2*$^{-/-}$, n=36 centrioles.

For each panel, representative U-ExM images of centrioles in S and G2 phase are shown. These are the same centrioles as in Figure 4G and were stained for alpha-tubulin (cyan), acetylated tubulin (yellow), and CEP135 (magenta). Scale bars = 1 um.

Graphs: Each column represents a centriole, for which the proximal and distal positions of CEP135 (magenta), acetylated tubulin (yellow) and alpha-tubulin (cyan) are displayed. Centrioles were arranged from shortest to longest. Numbers were adjusted for expansion factor. A line of best fit was added for CEP135 position: control procentrioles (dashed), *de novo* centrioles (dotted), and mutants (solid).

Figure 4 - Supplementary figure 4 – Quantification of SASS6 centriolar localization through S and G2 phase

Mutant centrioles have over-elongated SASS6. A) control procentrioles, n=53 centrioles; B) *de novo* centrioles, n=44 centrioles; C) *TUBD1*$^{-/-}$, n=39 centrioles; D) *TUBE1*$^{-/-}$, n=44 centrioles; E) *TEDC1*$^{-/-}$, n=34 centrioles; F) *TEDC2*$^{-/-}$, n=30 centrioles.

Each column represents a centriole, for which the proximal and distal positions of SASS6 (magenta) and alpha-tubulin (cyan) are displayed. Centrioles were arranged from shortest to longest. A Numbers were adjusted for expansion factor. line of best fit was added for SASS6 position: control procentrioles (dashed), *de novo* centrioles (dotted), and mutants (solid).

683
684 **Figure 4 - Supplementary figure 5 – Quantification of centriole widths and lengths**
685 Mutant centrioles have smaller widths compared to controls. A) control procentrioles, n=82
686 centrioles; B) *de novo* centrioles, n=86 centrioles; C) *TUBD1*$^{-/-}$, n=64 centrioles; D) *TUBE1*$^{-/-}$,
687 n=74 centrioles; E) *TEDC1*$^{-/-}$, n=56 centrioles; F) *TEDC2*$^{-/-}$, n=62 centrioles. Centriole widths and
688 lengths measured by alpha-tubulin antibody are graphed, adjusted for expansion factor. A line
689 of best fit was added (red).
690
691 **Fig 5. Mutant centrioles elongate further in mitosis before fragmenting**
692 U-ExM of centrioles stained for monoE (GT335, cyan), CP110 (yellow) and SASS6 (magenta).
693 **(A)** A prometaphase cell with centrioles formed *de novo* **(B)** An anaphase cell with centrioles
694 formed *de novo* **(C)** A prometaphase *TUBD1*$^{-/-}$ cell **(D)** A telophase *TUBD1*$^{-/-}$ cell **(E)** A
695 prometaphase *TUBE1*$^{-/-}$ cell **(F)** An anaphase *TUBE1*$^{-/-}$ cell. Scale bars: 1 um. Images were
696 acquired with a Yokogawa CSU-W1 SoRA with 2.8x relay.
697

698 ## Materials and Methods
699
700 **Cell lines and cell culture**
701 hTERT RPE-1 *TP53*$^{-/-}$ cells were a gift from Meng-Fu Bryan Tsou (Memorial Sloan Kettering
702 Cancer Center) and were cultured in DMEM/F-12 (Corning) supplemented with 10% Cosmic
703 Calf Serum (CCS; HyClone). HEK293T cells for lentivirus production (see below) were obtained
704 from the ATCC and cultured in DMEM (Corning) supplemented with 10% CCS. hTERT RPE-1
705 and HEK293T/17 cells were authenticated using STR profiling using CODIS loci. All other cell
706 lines used were derived from hTERT RPE-1 *TP53*$^{-/-}$ cells. Stable *TP53*$^{-/-}$*; TEDC1*$^{-/-}$ and
707 *TP53*$^{-/-}$*; TEDC2*$^{-/-}$ knockout cell lines were made in the hTERT RPE-1 *TP53*$^{-/-}$ cells by
708 CRISPR/Cas9 (see below). For rescue experiments, clonal knockout cell lines were rescued
709 using lentiviral transduction (see below). All cells were cultured at 37°C under 5% CO_2, and are
710 mycoplasma-free (Uphoff and Drexler, 2011).
711
712 **Generation of *TEDC1*$^{-/-}$ and *TEDC2*$^{-/-}$ cells and rescue cell lines**
713 *TEDC1*$^{-/-}$ and *TEDC2*$^{-/-}$ cells were generated by CRISPR/Cas9 mediated gene editing using a
714 recombinantly produced, purified Cas9 protein (Cas9-NLS, QB3 Macrolab, Berkeley) and
715 chemically synthetized two-component gRNA (crRNA:tracrRNA, Alt-R CRISPR-Cas9 system,
716 IDT). For increased efficiency, two gRNAs, both targeting the 5' end of each gene, were used at
717 the same time. Target sequences were: 5'-CGCCAAGTTCGACCGTCCGG-3' and 5'-
718 CGTCCAATCACCGCACGGGC-3' for TEDC1, and 5'-CGCACAGCGACAATTGCAAT-3' and 5'-
719 CACCGGCGCGAGCAGCCCGC-3' for TEDC2.
720
721 Lyophilized RNA oligos were reconstituted according to the instructions provided by the
722 manufacturer (IDT). Briefly, oligos were reconstituted in the duplex buffer at a concentration of
723 200 µM. To anneal crRNA with tracrRNA, 3 µl of each (600 pmol) were mixed, heated to 95°C,
724 and transferred to room temperature to gradually cool. Pre-complexed crRNA and tracrRNA
725 (550 pmol) were mixed with purified Cas9 (360 pmol), diluted with PBS to a total volume of 25 µl
726 and incubated for 15 min at room temperature to form ribonucloprotein complexes (RNPs).
727
728 RPE1 *TP53*$^{-/-}$ cells stably expressing GFP-centrin (Wang et al., 2017) were electroporated in a
729 home-made electroporation buffer (Zhang et al., 2014) using Amaxa Nucleofector II (Lonza).
730 Cells were electroporated with an equal mix of two RNPs: 50 µl of RNPs mixture was added to 2
731 x 10^6 cells in 200 µl electroporation buffer. To facilitate the identification of electroporated cells,
732 an mRuby2 expressing plasmid (pcDNA3-mRuby2, plasmid pTS3994) was electroporated
733 together with RNPs.
734
735 Two days after electroporation, cells expressing mRuby2 were sorted using FACS, and single
736 cells were plated into 96 well plates in conditioned media. Surviving clones were genotyped by
737 PCR of genomic DNA and screened for phenotype based on centrin-GFP expression.
738
739 Primers used for genotyping were: 5'CCCTGCCGACGCAGTGATTGG3' and
740 5'CAGGGAGTGGCGAGAGCACAC3' for TEDC1 and 5' CTTGCCCGCAAGGAGGGAGAGA3'
741 and 5'GCAGGGCCCAGCCCAAACAGA3' for TEDC2.

742
743 To rescue the mutations, Halo-3xFlag-tagged TEDC1 or APEX-V5-tagged TEDC2 were
744 introduced into the mutant cells using lentiviral transduction as described below.
745
746 **Lentivirus production and viral transduction**
747 Recombinant lentiviruses were made by cotransfection of HEK293T cells with the respective
748 transfer vectors (TEDC1-Halotag-3xFlag and TEDC2-V5-APEX2), second-generation lentiviral
749 cassettes (packaging vector psPAX2, pTS3312 and envelope vector pMD2.G, pTS3313) using
750 calcium phosphate-mediated transfection. Briefly, transfection mixture was made with CaCl2, 2x
751 HBS (50 mM Hepes, 10 mM KCl, 12 mM dextrose, 280 mM NaCl, 1.5 mM Na2HPO4x7H2O, pH
752 7.05), and plasmids. Cells were treated with 25 uM chloroquine immediately before transfection,
753 then the transfection mixture was added to cells. The medium was changed 5-6 h after
754 transfection, and viral supernatant was harvested after an additional 48 and 72 h. Recipient
755 cells (RPE-1 *TP53*$^{-/-}$*; TEDC1*$^{-/-}$ and *TP53*$^{-/-}$*; TEDC2*$^{-/-}$ and *TP53*$^{-/-}$*; TUBD1*$^{-/-}$ and *TP53*$^{-/-}$*;*
756 *TUBE1*$^{-/-}$) were transduced with viral supernatant and 8 ug/mL Sequabrene. Transduced cells
757 were expanded to 10-cm dishes.
758
759 **Immunofluorescence**
760 Cells were grown on poly-L-lysine-coated #1.5 glass coverslips (Electron Microscopy Sciences).
761 Cells were fixed with −20°C methanol for 15 min. Coverslips were then washed with PBS for 10
762 min and blocked with PBS-BT (3% BSA, 0.1% Triton X-100, 0.02% sodium azide in PBS) for 30
763 min. Coverslips were incubated with primary antibodies diluted in PBS-BT for 1 hr, washed with
764 PBS-BT, incubated with secondary antibodies and DAPI diluted in PBS-BT for 1 hr, then
765 washed again. Samples were mounted using Mowiol (Polysciences) in glycerol containing 1,4,-
766 diazobicycli-[2.2.2]octane (DABCO, Sigma-Aldrich) antifade.
767
768 **Cell cycle synchronization**
769 For cell cycle analyses in Fig 1, cells were seeded onto coverslips, then synchronized in G0/G1
770 by serum withdrawal for 24 hr, or in G2 with 10 μM RO-3306 (Adipogen) for 24 hr. Cells were
771 fixed for immunofluorescence and analyzed for centrin/CP110 presence.

772 For Fig 4 and 5, mitotic shakeoff was performed on asynchronously growing cells. One pre-
773 shake was performed to improve synchronization. Cells were fixed for U-ExM and expanded as
774 below.

775 **Expansion microscopy**
776 <u>Ultrastructure Expansion Microscopy (U-ExM)</u>
777 Cells were grown on poly-D-lysine-coated #1.5 glass coverslips (Electron Microscopy Sciences)
778 and fixed with −20°C methanol for 15 min, then washed with PBS. U-ExM was performed as
779 previously described (Gambarotto et al., 2019): coverslips were incubated overnight in an
780 acrylamide–formaldehyde anchoring solution (AA/FA; 0.7% formaldehyde, 1% acrylamide in
781 PBS) at 37°C. Gelation was allowed to proceed in monomer solution (19% sodium acrylate,
782 10% acrylamide, 0.1% bis-acrylamide, 0.5% ammonium persulfate-APS, 0.5% TEMED) for 1
783 hour at 37°C. Gels were heated in denaturation buffer (200 mM SDS, 200 mM NaCl, 50 mM
784 Tris-HCl pH 9) at 95°C for 1 h. After denaturation buffer was removed, gels were washed with
785 multiple water rinses and allowed to expand in water at room temperature overnight. Small

786 circles of each expanded gel (~5 mm in diameter) were excised and incubated with primary
787 antibodies diluted in PBS-BT (3% BSA, 0.1% Triton X-100 in PBS) on a nutator at 4°C
788 overnight. The next day, gels were washed three times with PBS-BT buffer and incubated with
789 secondary antibodies and 5 µg/ml DAPI diluted in PBS-BT, protected from light, on a nutator at
790 4°C overnight.
791
792 For Fig 4, Fig 4 – Supp 3 and Fig 4 – Supp 4 when co-staining with alpha-tubulin, centrioles
793 were fixed with 1.4% formaldehyde and 2% acrylamide for 3 to 5 hours at 37°C. U-ExM was
794 performed as described above. Gels were pre-incubated with anti alpha-tubulin antibody at 4°C
795 overnight prior to staining with other primary antibodies.
796
797 Expansion microscopy as per Kong et al.
798 For Fig 2 – Supp 1C, D, expansion microscopy was performed similar to (Kong et al., 2024).
799 Coverslips were incubated in 4% formaldehyde in 1x PBS for 1 hour. The coverslips were then
800 incubated overnight in an acrylamide–formaldehyde anchoring solution (AA/FA; 4%
801 formaldehyde, 30% acrylamide in PBS) at 40°C. Gelation was allowed to proceed in monomer
802 solution (7% sodium acrylate, 20% acrylamide, 0.04% bis-acrylamide, 0.5% ammonium
803 persulfate-APS, 0.5% TEMED in PBS) for 20 min on ice followed by 1 hour at room
804 temperature. Gels were heated in denaturation buffer (200 mM SDS, 200 mM NaCl, 50 mM Tris-
805 HCl pH 9) at 90°C for 1 h. After denaturation buffer was removed, gels were washed with
806 multiple water rinses and allowed to expand in water at room temperature overnight. Small
807 circles of each expanded gel (~5 mm in diameter) were excised and incubated with primary
808 antibodies diluted in PBS-BT (3% BSA, 0.1% Triton X-100 in PBS) on a nutator at 4°C
809 overnight. The next day, gels were washed three times with PBS-BT buffer and incubated with
810 secondary antibodies and 5 µg/ml DAPI diluted in PBS-BT, protected from light, on a nutator at
811 4°C overnight.
812
813 Expansion gel imaging (all protocols)
814 Immunostained gels were washed once with PBS and at least three times with water, and
815 placed in a glass-bottomed 35 mm plate for imaging. All U-ExM images were acquired as *z*-
816 stacks collected at 0.27-µm intervals using a confocal Zeiss Axio Observer microscope (Carl
817 Zeiss) with a PlanApoChromat 1.4 NA 63× oil immersion objective, a Yokogawa CSU-W1 (Fig
818 2) or Yokogawa CSU-W1 SoRA head with 2.8x relay (Fig 4, 5) and a Photometrics Prime BSI
819 express CMOS camera. Slidebook software (Intelligent Imaging Innovations, 3i) was used to
820 control the microscope system. Deconvolution was performed with Microvolution (Cupertino,
821 CA) using a calculated point spread function (PSF) for 10 iterations. ImageJ (FIJI) was used for
822 image analysis (Schindelin et al., 2012).
823
824 **Centriole measurements**
825 For measuring overall centriole width or length, z-stacks of U-ExM images were measured using
826 ImageJ (FIJI) on maximum projections. Only centrioles that were in perfect longitudinal or cross-
827 section were measured. Three measurements were made per centriole and averaged.
828 Measurements were adjusted for gel expansion factor. Statistical analysis was performed with
829 Graphpad Prism.
830
831 For measuring protein position as in Fig 4 – Supp 3 and Fig 4 – Supp 4, maximum projections of
832 U-ExM images of longitudinally positioned centrioles were measured using ImageJ (FIJI). The
833 coordinates of the proximal-most and distal-most position for each protein were recorded. Three
834 measurements were made per centriole and averaged. The recorded coordinates were used to

835 calculate the positions of the most proximal and most distal signal for each protein, then
836 graphed from shortest to longest centriole.
837
838 **Transmission electron microscopy.** For ultrastructural analysis of centrosomes by TEM,
839 RPE-1 *TP53*$^{-/-}$ *; TEDC1*$^{-/-}$ and RPE-1 *TP53*$^{-/-}$ *; TEDC2*$^{-/-}$ cells were synchronized in G2/M with 10
840 uM RO-3306 for 24 hrs. Cells were trypsinized, resuspended in complete media and centrifuged
841 at 800g for 5 min. The pellet was collected in a 14-mL tube and fixed in 2%
842 paraformaldehyde/2.5% glutaraldehyde (Ted Pella Inc., Redding, CA) in 100 mM cacodylate
843 buffer, pH 7.2 for 2 hr at room temperature. Samples were washed in cacodylate buffer and
844 postfixed in 1% osmium tetroxide (Ted Pella Inc.)/1.5% potassium ferricyanide (Sigma, St.
845 Louis, MO) for 1 hr. Samples were then rinsed extensively in dH_2O prior to en bloc staining with
846 1% aqueous uranyl acetate (Ted Pella Inc.) for 1 hr. Following several rinses in dH_2O, samples
847 were dehydrated in a graded series of ethanol and embedded in Eponate 12 resin (Ted Pella
848 Inc.). Ultrathin sections of 95 nm were cut with a Leica Ultracut UCT ultramicrotome (Leica
849 Microsystems Inc., Bannockburn, IL), stained with uranyl acetate and lead citrate, and viewed
850 on a JEOL 1200 EX transmission electron microscope (JEOL USA Inc., Peabody, MA)
851 equipped with an AMT 8 megapixel digital camera and AMT Image Capture Engine V602
852 software (Advanced Microscopy Techniques, Woburn, MA).
853
854 Symmetrization of TEM images was performed with centrioleJ (https://www.epfl.ch/labs/gonczy-
855 lab/databases-and-resources/ressources-centriolej/).
856
857 **TEDC1 and TEDC2 pulldowns**
858 Cells stably expressing TEDC1-Halotag-3xFlag or TEDC2-V5-APEX2 were lysed in 50 mM Tris
859 pH7.5, 150 mM NaCl, 1% Triton X-100, 1 mM DTT, Halt protease and phosphatase inhibitor
860 cocktail (ThermoFisher Scientific) for 30 minutes on ice, then cleared by centrifugation at 21,000
861 g for 20 min. Protein concentration was determined by Pierce BCA Protein Assay - Reducing
862 Agent Compatible (ThermoFisher Scientific). Each cell lysate was incubated with 25 uL of
863 equilibrated Chromotek Halo-Trap Magnetic Agarose (Proteintech) or Chromotek V5-Trap
864 Magnetic Agarose (Proteintech) for 1 h at 4C on a nutator. Beads were washed using a
865 magnetic separator rack. Elution was performed by adding 80 uL of 2x SDS loading buffer (100
866 mM Tris pH 6.8, 4% SDS, 20% glycerol, 100 mM DTT), boiling the beads for 5 min at 95C, then
867 separating the eluate with a magnetic separator rack. Samples were loaded on SDS-PAGE and
868 transferred for Western blotting.
869
870 **Western blotting**
871 For Fig 4 - Supp 2, samples were lysed in 50 mM Tris pH7.5, 150 mM NaCl, 1% Triton X-100, 1
872 mM DTT, Halt protease and phosphatase inhibitor cocktail (ThermoFisher Scientific) for 30
873 minutes on ice, then cleared by centrifugation at 21,000 g for 20 min. Protein concentration was
874 determined by Pierce BCA Protein Assay - Reducing Agent Compatible (ThermoFisher
875 Scientific). Equal amounts of protein (20 to 40 ug) were loaded per lane. For Fig 3, samples
876 were loaded after pulldowns.
877

878 Proteins were separated by SDS-PAGE and transferred to nitrocellulose (LiCOR Biosciences) in
879 transfer buffer (192 mM Glycine, 25 mM Tris, 20% ethanol). Membranes were blocked with 5%
880 milk in TBST (137 mM NaCl, 25 mM Tris, 2.7 mM KCl, 0.1% Tween-20) at room temp for 1 h,
881 then washed three times with TBST for 5 min each wash. Membranes were incubated with
882 primary antibodies overnight at 4C on a nutator. The next day, membranes were washed three
883 times with TBST for 5 min each wash and incubated with secondary antibodies at room
884 temperature for 2.5 hours. Membranes were washed again with TBST for 5 min each wash and
885 then imaged with the LiCOR Odyssey XF imager and analyzed using Image Studio (LiCOR
886 Biosciences). Each experiment was performed in triplicate.
887
888 **Antibodies**
889 Primary antibodies used for immunofluorescence and U-ExM and dilutions in PBS-BT: mouse
890 IgG2b anti-acetylated-tubulin, clone 6-11B-1 (1:1000,Sigma-Aldrich Cat# T6793,
891 RRID:AB_477585), rabbit anti-acetyl-α-tubulin (Lys40) (1:100, Cell Signaling Technology Cat#
892 5335, RRID:AB_10544694), mouse IgG2b anti-centrin3, clone 3e6 (1:1000, Novus Biological,
893 RRID:AB_537701), mouse IgG2a anti-centrin, clone 20H5 (IF 1:200, UExM 1:500, EMD
894 Millipore, RRID:AB_10563501), rat anti-Cep120 (1:1000, gift from Moe Mahjoub (Betleja et al.,
895 2018)), rabbit anti-Cep135 (1:500, Proteintech Cat# 24428-1-AP, RRID:AB_2879543), rabbit
896 anti-Cep295 (1:1000, Sigma-Aldrich Cat# HPA038596, RRID:AB_10672720), rabbit anti-Cep44
897 (1:100, Proteintech Cat# 24457-1-AP, RRID:AB_2879557), rabbit anti-CENPJ (1:500,
898 Proteintech Cat# 11517-1-AP, RRID:AB_2244605), rabbit anti-CP110 (IF 1:200, UExM 1:2000,
899 Proteintech Cat# 12780-1-AP, RRID:AB_10638480), mouse IgG1 anti-Flag, clone M2 (1:500,
900 Sigma-Aldrich Cat# F1804, RRID:AB_262044), mouse IgG1 anti-gamma-tubulin, clone GTU-88
901 (IF 1:1000, UExM 1:500, Sigma-Aldrich, RRID:AB_477584), mouse IgG2a anti-PCNA (1:500,
902 BioLegend, RRID:AB_314692), rabbit anti-POC5 (for IF: 1:500, Bethyl Laboratories,
903 RRID:AB_10949152), rabbit anti-POC5 (for U-ExM: 1:500, Thermo Fisher Scientific Cat# A303-
904 341A (also A303-341A-T), RRID:AB_10971172), mouse IgG1 anti-polyglutamylation, clone
905 GT335 (1:500, AdipoGen Cat# AG-20B-0020, RRID:AB_2490210), rabbit anti-polyglutamate-
906 chain, polyE (1:500, AdipoGen Cat# AG-25B-0030, RRID:AB_2490540), mouse IgG2b anti-
907 SASS6 (1:200, Santa Cruz Cat# sc-81431, RRID:AB_1128357), rabbit anti-STIL (1:500, Abcam
908 Cat# ab89314, RRID:AB_2197878), mouse IgG2a anti-V5 (1:00, Thermo Fisher Scientific Cat#
909 R960-25, RRID:AB_2556564), rabbit anti-WDR90 (1:100, Thermo Fisher Scientific Cat# PA5-
910 61943, RRID:AB_2649628), chicken anti-GFP antibody (Aves Cat #GFP-1020,
911 RRID:AB_10000240).
912
913 For immunofluorescence and U-ExM, AlexaFluor conjugated secondary antibodies (Thermo-
914 Fisher) were diluted 1:1000 in PBS-BT. Goat anti-Mouse IgG1, 488 (1:1000, Thermo Fisher
915 Scientific Cat# A-21121, RRID:AB_2535764), Goat anti-Mouse IgG2a, 488 (1:1000, Thermo
916 Fisher Scientific Cat# A-21131, RRID:AB_2535771), Goat anti-Mouse IgG2b, 488 (1:1000,
917 Thermo Fisher Scientific Cat# A-21141, RRID:AB_2535778), Goat anti-rabbit IgG (H+L), 488
918 (1:1000, Thermo Fisher Scientific Cat# A-11034 (also A11034), RRID:AB_2576217), Goat anti-
919 Mouse IgG1, 568 (1:500, Thermo Fisher Scientific Cat# A-21124, RRID:AB_2535766), Goat
920 anti-Mouse IgG2a, 568 (1:500, Thermo Fisher Scientific Cat# A-21134, RRID:AB_2535773),
921 Goat anti-Mouse IgG2b, 568 (1:500, Thermo Fisher Scientific Cat# A-21144,

RRID:AB_2535780), Goat anti-rabbit IgG (H+L), 568 (1:500, Thermo Fisher Scientific Cat# A-11036 (also A11036), RRID:AB_10563566), Goat anti-Mouse IgG3, 594 (1:500, Thermo Fisher Scientific Cat# A-21155, RRID:AB_2535785), Goat anti-rat IgG (H+L), 594 (1:500,Thermo Fisher Scientific Cat# A-11007 (also A11007), RRID:AB_10561522), Goat anti-Mouse IgG1, 647 (1:500, Thermo Fisher Scientific Cat# A-21240, RRID:AB_2535809), Goat anti-Mouse IgG2a, 647 (1:500, Thermo Fisher Scientific Cat# A-21241, RRID:AB_2535810), Goat anti-Mouse IgG2b, 647 (1:500, Thermo Fisher Scientific Cat# A-21242, RRID:AB_2535811), Goat anti-rabbit IgG (H+L), 647 (1:500, Thermo Fisher Scientific Cat# A32733, RRID:AB_2633282), Goat anti-Mouse, Star Red (1:200, Abberior Cat# STRED-1001, RRID:AB_3068620), Goat anti-rabbit, Star Orange (1:200, Abberior Cat #STORANGE-1002, RRID:AB_3068622), Goat anti-chicken, Alexa 488 (Thermo Fisher Scientific Cat# A-11039, RRID:AB_2534096).

Primary antibodies used for Western blotting and dilutions in TBST: rabbit anti TUBD1 (1:1000, Sigma-Aldrich Cat# HPA027090, RRID:AB_1858457), rabbit anti TUBE1 (1:1000, Sigma-Aldrich Cat # HPA032074, RRID:AB_10601216), rabbit anti C14orf80 (1:1000, Sigma-Aldrich Cat # HPA039049, RRID:AB_2676320), rabbit anti C16orf59 (1:1000, Sigma-Aldrich Cat # HPA055389, RRID:AB_2732595), mouse IgG2b anti SASS6 (1:200, Santa Cruz Biotech Cat # sc-81431, RRID:AB_1128357), rabbit anti STIL (1:2000, Abcam Cat# ab89314, RRID:AB_2197878), rabbit anti CENPJ/CPAP (1:1000, Proteintech Cat# 11517-1-AP, RRID:AB_2244605), rabbit anti POC5 (1:1000, Thermo Fisher Scientific Cat# A303-341A (also A303-341A-T), RRID:AB_10971172), mouse IgG2a anti V5 (1:1000, Thermo Fisher Scientific Cat# R960-25, RRID:AB_2556564), mouse IgG1 anti Flag, clone M2 (1:2000, Sigma-Aldrich Cat# F1804, RRID:AB_262044). Secondary antibodies used for Western blotting: 680 Donkey anti rabbit (H+L) (1:20,000, Thermo Fisher Scientific Cat# A10043, RRID:AB_2534018), 800 Donkey anti rabbit (H+L) (1:20,000, Li-COR Cat# 926-32213, RRID:AB_621848), 680 Donkey anti mouse (H+L) (1:20,000, Thermo Fisher Scientific Cat# A10038, RRID:AB_11180593), 800 Donkey anti mouse (H+L) (1:20,000, Li-COR Cat# 926-32212, RRID:AB_621847).

Acknowlegments

This work was supported by NIH/NIGMS (K99/R00 GM131024 to J.T.W. and R35 GM130286 to T.S.) and Washington University in St. Louis startup funds (to J.T.W). We thank Wandy Beatty of the Washington University Molecular Microbiology Imaging Facility for assistance with transmission electron microscopy, Moe Mahjoub (Washington University School of Medicine) for the gift of the CEP120 and goat anti-rat antibodies, and Meng-Fu Bryan Tsou (Memorial Sloan Kettering Cancer Center) for the gifts of RPE-1 *TP53*$^{-/-}$ and RPE-1 *TP53*$^{-/-}$ *; SASS6*$^{-/-}$ cells. We thank the Stanford cytoskeleton group, WashU centrosome/cilia group, members of the Stearns lab, and David Breslow for helpful discussions. We also thank Hani Zaher's and Joe Jez's labs for hosting the Wang lab during renovations and Larry Galloway for help with Python.

References

Abramson, J., Adler, J., Dunger, J., Evans, R., Green, T., Pritzel, A., Ronneberger, O., Willmore, L., Ballard, A. J., Bambrick, J., et al. (2024). Accurate structure prediction of biomolecular interactions with AlphaFold 3. *Nature* 630, 493–500.

Arslanhan, M. D., Cengiz-Emek, S., Odabasi, E., Steib, E., Hamel, V., Guichard, P. and Firat-Karalar, E. N. (2023). CCDC15 localizes to the centriole inner scaffold and controls centriole length and integrity. *Journal of Cell Biology* 222, e202305009.

Bournonville, L., Laporte, Marine. H., Borgers, S., Guichard, P. and Hamel, V. (2024). The A-C Linker controls centriole cohesion and duplication.

Breslow, D. K. and Holland, A. J. (2019). Mechanism and Regulation of Centriole and Cilium Biogenesis. *Annu. Rev. Biochem.* 88, 691–724.

Breslow, D. K., Hoogendoorn, S., Kopp, A. R., Morgens, D. W., Vu, B. K., Kennedy, M. C., Han, K., Li, A., Hess, G. T., Bassik, M. C., et al. (2018). A CRISPR-based screen for Hedgehog signaling provides insights into ciliary function and ciliopathies. *Nat Genet* 50, 460–471.

Comartin, D., Gupta, G. D., Fussner, E., Coyaud, É., Hasegan, M., Archinti, M., Cheung, S. W. T., Pinchev, D., Lawo, S., Raught, B., et al. (2013). CEP120 and SPICE1 Cooperate with CPAP in Centriole Elongation. *Current Biology* 23, 1360–1366.

de Loubresse, N. G., Ruiz, F. and Beisson, J. (2001). Role of delta-tubulin and the C-tubule in assembly of Paramecium basal bodies. *BMC Cell Biology* 7.

Dupuis-Williams, P., Fleury-Aubusson, A., de Loubresse, N. G., Geoffroy, H., Vayssié, L., Galvani, A., Espigat, A. and Rossier, J. (2002). Functional role of ε-tubulin in the assembly of the centriolar microtubule scaffold. *Journal of Cell Biology* 158, 1183–1193.

Dutcher, S. K. and Trabuco, E. C. (1998). The UNI3 Gene Is Required for Assembly of Basal Bodies of Chlamydomonas and Encodes ʕ-Tubulin, a New Member of the Tubulin Superfamily. *Molecular Biology of the Cell* 9, 16.

Dutcher, S. K., Morrissette, N. S., Preble, A. M., Rackley, C. and Stanga, J. (2002). ᔑ-Tubulin Is an Essential Component of the Centriole. *Molecular Biology of the Cell* 13, 11.

Evans, R., O'Neill, M., Pritzel, A., Antropova, N., Senior, A., Green, T., Žídek, A., Bates, R., Blackwell, S., Yim, J., et al. (2021). *Protein complex prediction with AlphaFold-Multimer*. Bioinformatics.

Farrell, K., Wang, J. T. and Stearns, T. (2024). Spindle assembly checkpoint-dependent mitotic delay is required for cell division in absence of centrosomes.

Gadelha, C., Wickstead, B., McKean, P. G. and Gull, K. (2006). Basal body and flagellum mutants reveal a rotational constraint of the central pair microtubules in the axonemes of trypanosomes. *Journal of Cell Science* 119, 2405–2413.

997 Gambarotto, D., Zwettler, F. U., Le Guennec, M., Schmidt-Cernohorska, M., Fortun, D.,
998 Borgers, S., Heine, J., Schloetel, J.-G., Reuss, M., Unser, M., et al. (2019). Imaging
999 cellular ultrastructures using expansion microscopy (U-ExM). *Nat Methods* 16, 71–74.

1000 González, C., Tavosanis, G. and Mollinari, C. (1998). Centrosomes and microtubule
1001 organisation during *Drosophila* development. *Journal of Cell Science* 111, 2697–2706.

1002 Goodenough, U. W. and StClair, H. S. (1975). BALD-2: a mutation affecting the formation of
1003 doublet and triplet sets of microtubules in Chlamydomonas reinhardtii. *Journal of Cell*
1004 *Biology* 66, 480–491.

1005 Guichard, P. and Gönczy, P. (2016). Basal body structure in Trichonympha. *Cilia* 5, 9.

1006 Guichard, P., Desfosses, A., Maheshwari, A., Hachet, V., Dietrich, C., Brune, A., Ishikawa, T.,
1007 Sachse, C. and Gönczy, P. (2012). Cartwheel Architecture of *Trichonympha* Basal Body.
1008 *Science* 337, 553–553.

1009 Guichard, P., Laporte, M. H. and Hamel, V. (2023). The centriolar tubulin code. *Seminars in Cell*
1010 *& Developmental Biology* 137, 16–25.

1011 Hamel, V., Steib, E., Hamelin, R., Armand, F., Borgers, S., Flückiger, I., Busso, C., Olieric, N.,
1012 Sorzano, C. O. S., Steinmetz, M. O., et al. (2017). Identification of Chlamydomonas
1013 Central Core Centriolar Proteins Reveals a Role for Human WDR90 in Ciliogenesis.
1014 *Current Biology* 27, 2486-2498.e6.

1015 Hatzopoulos, G. N., Erat, M. C., Cutts, E., Rogala, K. B., Slater, L. M., Stansfeld, P. J. and
1016 Vakonakis, I. (2013). Structural Analysis of the G-Box Domain of the Microcephaly
1017 Protein CPAP Suggests a Role in Centriole Architecture. *Structure* 21, 2069–2077.

1018 Hilbert, M., Noga, A., Frey, D., Hamel, V., Guichard, P., Kraatz, S. H. W., Pfreundschuh, M.,
1019 Hosner, S., Flückiger, I., Jaussi, R., et al. (2016). SAS-6 engineering reveals
1020 interdependence between cartwheel and microtubules in determining centriole
1021 architecture. *Nat Cell Biol* 18, 393–403.

1022 Huttlin, E. L., Bruckner, R. J., Paulo, J. A., Cannon, J. R., Ting, L., Baltier, K., Colby, G.,
1023 Gebreab, F., Gygi, M. P., Parzen, H., et al. (2017). Architecture of the human
1024 interactome defines protein communities and disease networks. *Nature* 545, 505–509.

1025 Huttlin, E. L., Bruckner, R. J., Navarrete-Perea, J., Cannon, J. R., Baltier, K., Gebreab, F., Gygi,
1026 M. P., Thornock, A., Zarraga, G., Tam, S., et al. (2021). Dual proteome-scale networks
1027 reveal cell-specific remodeling of the human interactome. *Cell* 184, 3022-3040.e28.

1028 Izquierdo, D., Wang, W.-J., Uryu, K. and Tsou, M.-F. B. (2014). Stabilization of Cartwheel-less
1029 Centrioles for Duplication Requires CEP295-Mediated Centriole-to-Centrosome
1030 Conversion. *Cell Reports* 8, 957–965.

1031 Junker, A. D., Woodhams, L. G., Soh, A. W. J., O'Toole, E. T., Bayly, P. V. and Pearson, C. G.
1032 (2022). Basal bodies bend in response to ciliary forces. *MBoC* 33, ar146.

1033 Kann, M., Soues, S., Levilliers, N. and Fouquet, J. (2003). Glutamylated tubulin: Diversity of
1034 expression and distribution of isoforms. *Cell Motil. Cytoskeleton* 55, 14–25.

1035 Klena, N., Le Guennec, M., Tassin, A., Van Den Hoek, H., Erdmann, P. S., Schaffer, M.,
1036 Geimer, S., Aeschlimann, G., Kovacik, L., Sadian, Y., et al. (2020). Architecture of the
1037 centriole cartwheel-containing region revealed by cryo-electron tomography. *The EMBO*
1038 *Journal* 39, e106246.

1039 Kleylein-Sohn, J., Westendorf, J., Le Clech, M., Habedanck, R., Stierhof, Y.-D. and Nigg, E. A.
1040 (2007). Plk4-Induced Centriole Biogenesis in Human Cells. *Developmental Cell* 13, 190–
1041 202.

1042 Kong, D., Sahabandu, N., Sullenberger, C., Vásquez-Limeta, A., Luvsanjav, D., Lukasik, K. and
1043 Loncarek, J. (2020). Prolonged mitosis results in structurally aberrant and over-
1044 elongated centrioles. *Journal of Cell Biology* 219, e201910019.

1045 Kong, D., Luvsanjav, D. and Loncarek, J. (2024). Immunolabel-First-Expand-Later Expansion
1046 Microscopy Approach Using Stable STED Dyes. *Methods Mol Biol* 2725, 89–101.

1047 Kraatz, S., Guichard, P., Obbineni, J. M., Olieric, N., Hatzopoulos, G. N., Hilbert, M., Sen, I.,
1048 Missimer, J., Gönczy, P. and Steinmetz, M. O. (2016). The Human Centriolar Protein
1049 CEP135 Contains a Two-Stranded Coiled-Coil Domain Critical for Microtubule Binding.
1050 *Structure* 24, 1358–1371.

1051 Kumar, D., Rains, A., Herranz-Pérez, V., Lu, Q., Shi, X., Swaney, D. L., Stevenson, E., Krogan,
1052 N. J., Huang, B., Westlake, C., et al. (2021). A ciliopathy complex builds distal
1053 appendages to initiate ciliogenesis. *Journal of Cell Biology* 220, e202011133.

1054 Laporte, M. H., Bouhlel, I. B., Bertiaux, E., Morrison, C. G., Giroud, A., Borgers, S., Azimzadeh,
1055 J., Bornens, M., Guichard, P., Paoletti, A., et al. (2022). Human SFI1 and Centrin form a
1056 complex critical for centriole architecture and ciliogenesis. *The EMBO Journal* 41,
1057 e112107.

1058 Laporte, M. H., Gambarotto, D., Bertiaux, É., Bournonville, L., Louvel, V., Nunes, J. M., Borgers,
1059 S., Hamel, V. and Guichard, P. (2024). Time-series reconstruction of the molecular
1060 architecture of human centriole assembly. *Cell* 187, 2158-2174.e19.

1061 Le Borgne, P., Greibill, L., Laporte, M. H., Lemullois, M., Bouhouche, K., Temagoult, M.,
1062 Rosnet, O., Le Guennec, M., Lignières, L., Chevreux, G., et al. (2022). The evolutionary
1063 conserved proteins CEP90, FOPNL, and OFD1 recruit centriolar distal appendage
1064 proteins to initiate their assembly. *PLoS Biol* 20, e3001782.

1065 Le Guennec, M., Klena, N., Gambarotto, D., Laporte, M. H., Tassin, A.-M., Van Den Hoek, H.,
1066 Erdmann, P. S., Schaffer, M., Kovacik, L., Borgers, S., et al. (2020). A helical inner
1067 scaffold provides a structural basis for centriole cohesion. *Sci. Adv.* 6, eaaz4137.

1068 LeGuennec, M., Klena, N., Aeschlimann, G., Hamel, V. and Guichard, P. (2021). Overview of
1069 the centriole architecture. *Current Opinion in Structural Biology* 66, 58–65.

1070 Lin, Y.-C., Chang, C.-W., Hsu, W.-B., Tang, C.-J. C., Lin, Y.-N., Chou, E.-J., Wu, C.-T. and
1071 Tang, T. K. (2013a). Human microcephaly protein CEP135 binds to hSAS-6 and CPAP,
1072 and is required for centriole assembly. *EMBO J* 32, 1141–1154.

1073 Lin, Y.-N., Wu, C.-T., Lin, Y.-C., Hsu, W.-B., Tang, C.-J. C., Chang, C.-W. and Tang, T. K.
1074 (2013b). CEP120 interacts with CPAP and positively regulates centriole elongation.
1075 *Journal of Cell Biology* 202, 211–219.

1076 Mahecic, D., Gambarotto, D., Douglass, K. M., Fortun, D., Banterle, N., Ibrahim, K. A., Le
1077 Guennec, M., Gönczy, P., Hamel, V., Guichard, P., et al. (2020). Homogeneous
1078 multifocal excitation for high-throughput super-resolution imaging. *Nat Methods* 17, 726–
1079 733.

1080 Mahjoub, M. R., Xie, Z. and Stearns, T. (2010). Cep120 is asymmetrically localized to the
1081 daughter centriole and is essential for centriole assembly. *Journal of Cell Biology* 191,
1082 331–346.

1083 Pelletier, L., O'Toole, E., Schwager, A., Hyman, A. A. and Müller-Reichert, T. (2006). Centriole
1084 assembly in Caenorhabditis elegans. *Nature* 444, 619–623.

1085 Pierron, M., Woglar, A., Busso, C., Jha, K., Mikeladze-Dvali, T., Croisier, M. and Gönczy, P.
1086 (2023). Centriole elimination during *Caenorhabditis elegans* oogenesis initiates with loss
1087 of the central tube protein SAS -1. *The EMBO Journal* 42, e115076.

1088 Pimenta-Marques, A., Bento, I., Lopes, C. a. M., Duarte, P., Jana, S. C. and Bettencourt-Dias,
1089 M. (2016). A mechanism for the elimination of the female gamete centrosome in
1090 Drosophila melanogaster. *Science* 353, aaf4866.

1091 Ross, I., Clarissa, C., Giddings, T. H. and Winey, M. (2013). ε-tubulin is essential in
1092 *Tetrahymena thermophila* for the assembly and stability of basal bodies. *Journal of Cell*
1093 *Science* jcs.128694.

1094 Sahabandu, N., Kong, D., Magidson, V., Nanjundappa, R., Sullenberger, C., Mahjoub, M. R.
1095 and Loncarek, J. (2019). Expansion microscopy for the analysis of centrioles and cilia.
1096 *Journal of Microscopy* 276, 145–159.

1097 Sala, C., Würtz, M., Atorino, E. S., Neuner, A., Partscht, P., Hoffmann, T., Eustermann, S. and
1098 Schiebel, E. (2024). An interaction network of inner centriole proteins organised by
1099 POC1A-POC1B heterodimer crosslinks ensures centriolar integrity. *Nat Commun* 15,
1100 9857.

1101 Schindelin, J., Arganda-Carreras, I., Frise, E., Kaynig, V., Longair, M., Pietzsch, T., Preibisch,
1102 S., Rueden, C., Saalfeld, S., Schmid, B., et al. (2012). Fiji: an open-source platform for
1103 biological-image analysis. *Nat Methods* 9, 676–682.

1104 Schweizer, N., Haren, L., Dutto, I., Viais, R., Lacasa, C., Merdes, A. and Lüders, J. (2021). Sub-
1105 centrosomal mapping identifies augmin-γTuRC as part of a centriole-stabilizing scaffold.
1106 *Nat Commun* 12, 6042.

1107 Sharma, A., Aher, A., Dynes, N. J., Frey, D., Katrukha, E. A., Jaussi, R., Grigoriev, I., Croisier,
1108 M., Kammerer, R. A., Akhmanova, A., et al. (2016). Centriolar CPAP/SAS-4 Imparts
1109 Slow Processive Microtubule Growth. *Developmental Cell* 37, 362–376.

1110 Spektor, A., Tsang, W. Y., Khoo, D. and Dynlacht, B. D. (2007). Cep97 and CP110 Suppress a
1111 Cilia Assembly Program. *Cell* 130, 678–690.

1112 Steib, E., Laporte, M. H., Gambarotto, D., Olieric, N., Zheng, C., Borgers, S., Olieric, V., Le
1113 Guennec, M., Koll, F., Tassin, A.-M., et al. (2020). WDR90 is a centriolar microtubule
1114 wall protein important for centriole architecture integrity. *eLife* 9, e57205.

1115 Sullenberger, C., Vasquez-Limeta, A., Kong, D. and Loncarek, J. (2020). With Age Comes
1116 Maturity: Biochemical and Structural Transformation of a Human Centriole in the Making.
1117 *Cells* 9, 1429.

1118 Tischer, J., Carden, S. and Gergely, F. (2021). Accessorizing the centrosome: new insights into
1119 centriolar appendages and satellites. *Current Opinion in Structural Biology* 66, 148–155.

1120 Uphoff, C. C. and Drexler, H. G. (2011). Detecting Mycoplasma Contamination in Cell Cultures
1121 by Polymerase Chain Reaction. In *Cancer Cell Culture* (ed. Cree, I. A.), pp. 93–103.
1122 Totowa, NJ: Humana Press.

1123 Van Dijk, J., Rogowski, K., Miro, J., Lacroix, B., Eddé, B. and Janke, C. (2007). A Targeted
1124 Multienzyme Mechanism for Selective Microtubule Polyglutamylation. *Molecular Cell* 26,
1125 437–448.

1126 Vásquez-Limeta, A., Lukasik, K., Kong, D., Sullenberger, C., Luvsanjav, D., Sahabandu, N.,
1127 Chari, R. and Loncarek, J. (2022). CPAP insufficiency leads to incomplete centrioles that
1128 duplicate but fragment. *Journal of Cell Biology* 221, e202108018.

1129 Wang, J. T. and Stearns, T. (2017). The ABCs of Centriole Architecture: The Form and Function
1130 of Triplet Microtubules. *Cold Spring Harb Symp Quant Biol* 82, 145–155.

1131 Wang, W.-J., Acehan, D., Kao, C.-H., Jane, W.-N., Uryu, K. and Tsou, M.-F. B. (2015). De novo
1132 centriole formation in human cells is error-prone and does not require SAS-6 self-
1133 assembly. *eLife* 4, e10586.

1134 Wang, J. T., Kong, D., Hoerner, C. R., Loncarek, J. and Stearns, T. (2017). Centriole triplet
1135 microtubules are required for stable centriole formation and inheritance in human cells.
1136 *eLife* 6, e29061.

1137 Woglar, A., Pierron, M., Schneider, F. Z., Jha, K., Busso, C. and Gönczy, P. (2022). Molecular
1138 architecture of the C. elegans centriole. *PLoS Biol* 20, e3001784.

1139 Zhang, Y., Vanoli, F., LaRocque, J. R., Krawczyk, P. M. and Jasin, M. (2014). Biallelic targeting
1140 of expressed genes in mouse embryonic stem cells using the Cas9 system. *Methods* 69,
1141 171–178.

1142

Figure 1

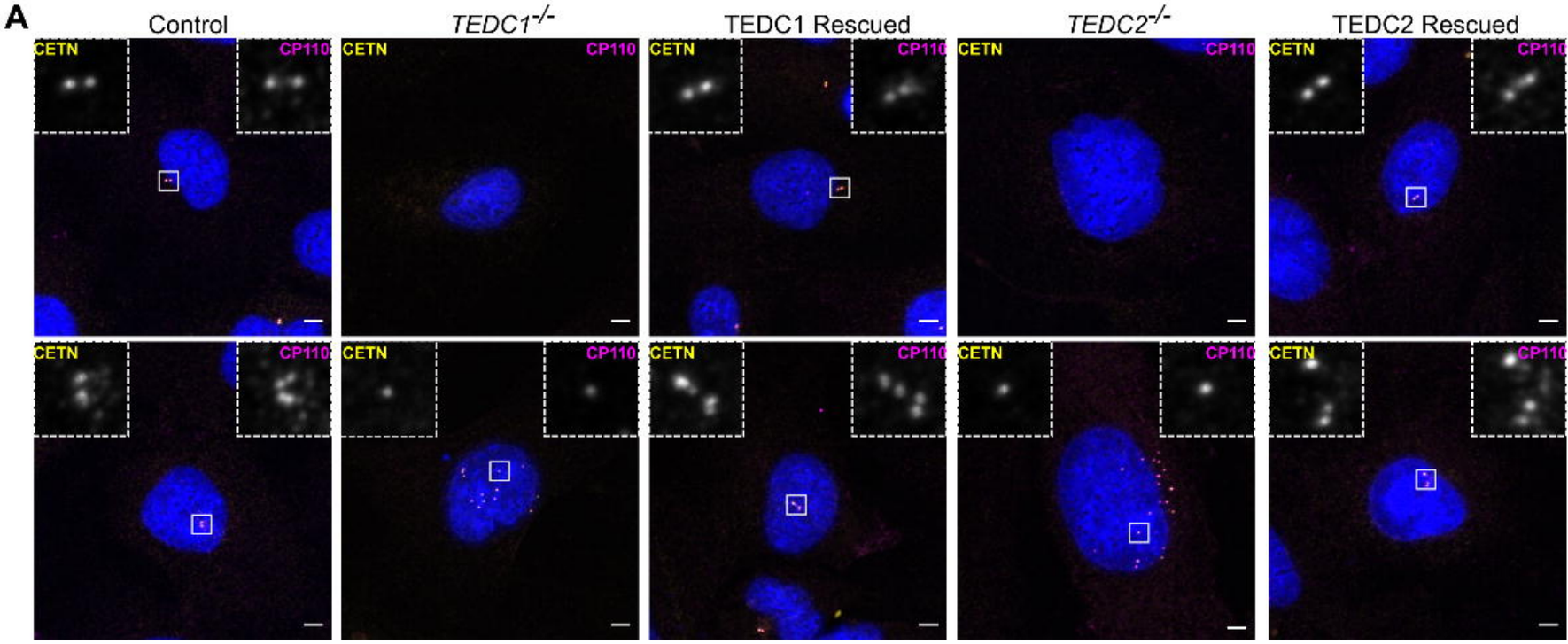
A
Control
TEDC1-/-
TEDC1 Rescued
TEDC2-/-
TEDC2 Rescued
CETN
CP110

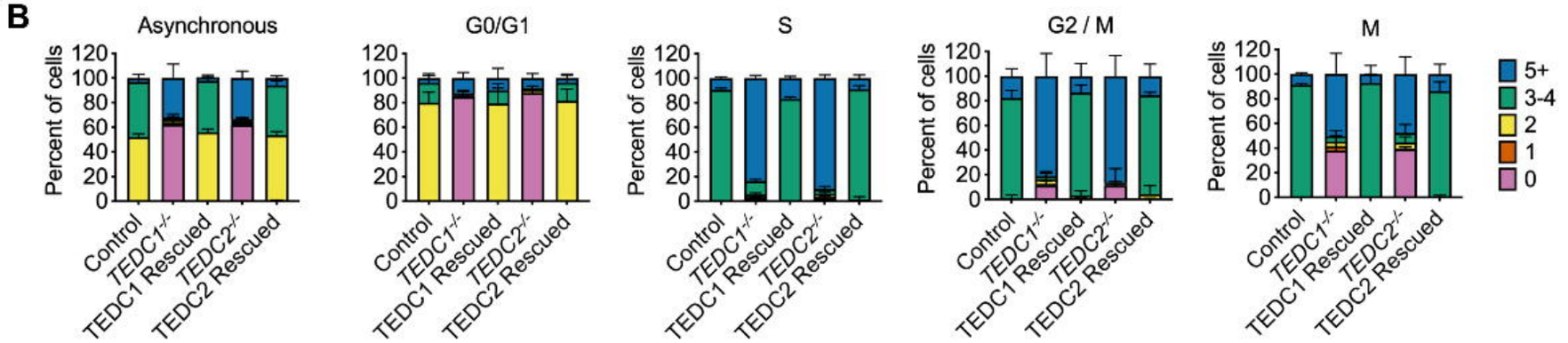
B
Asynchronous
G0/G1
S
G2 / M
M
Percent of cells
0
20
40
60
80
100
120
Control
TEDC1-/-
TEDC1 Rescued
TEDC2-/-
TEDC2 Rescued
5+
3-4
2
1
0

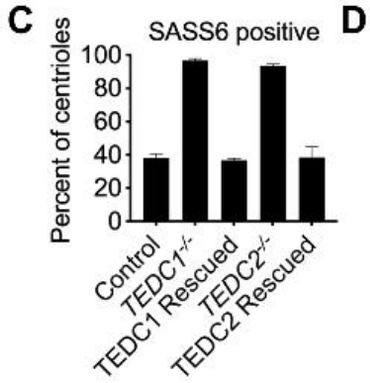
C
SASS6 positive
Percent of centrioles
0
20
40
60
80
100
Control
TEDC1-/-
TEDC1 Rescued
TEDC2-/-
TEDC2 Rescued

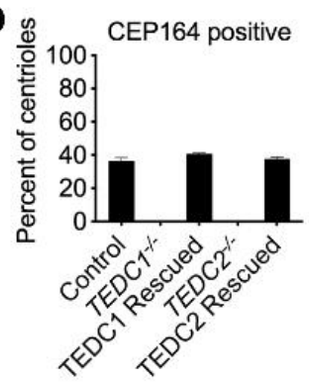
D
CEP164 positive
Percent of centrioles
0
20
40
60
80
100
Control
TEDC1-/-
TEDC1 Rescued
TEDC2-/-
TEDC2 Rescued

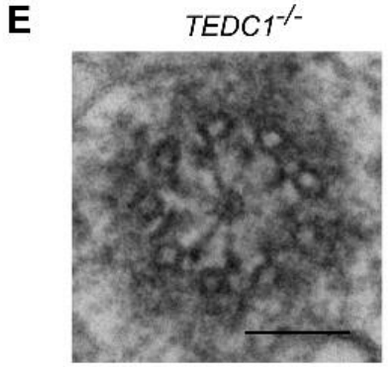
E
TEDC1-/-

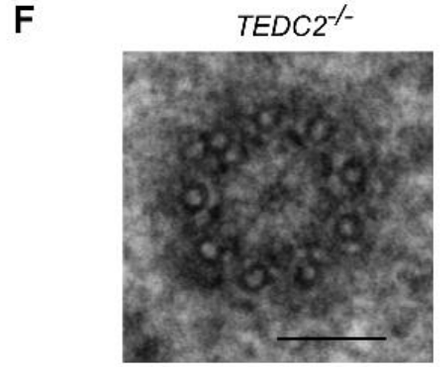
F
TEDC2-/-

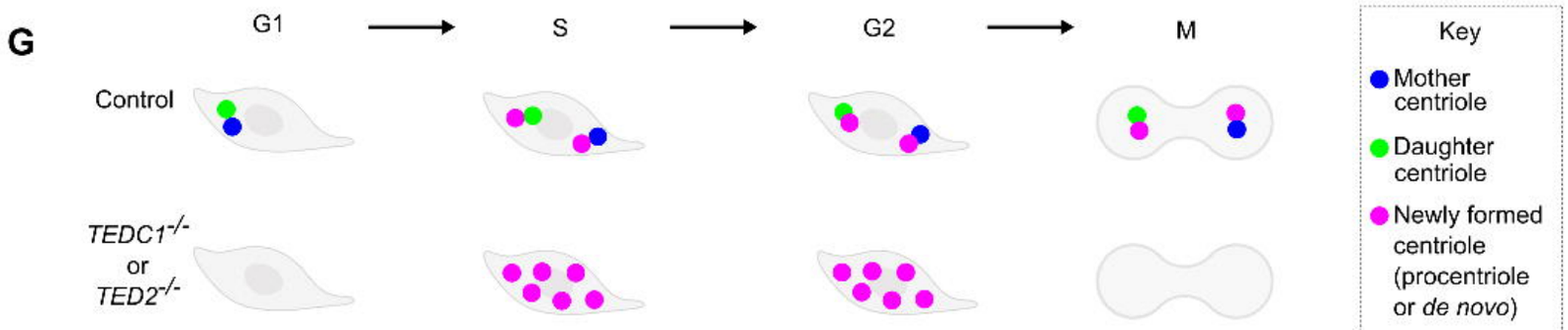
G
G1
S
G2
M
Control
TEDC1-/-
or
TED2-/-
Key
Mother centriole
Daughter centriole
Newly formed centriole (procentriole or de novo)

Figure 1 - Supp 1

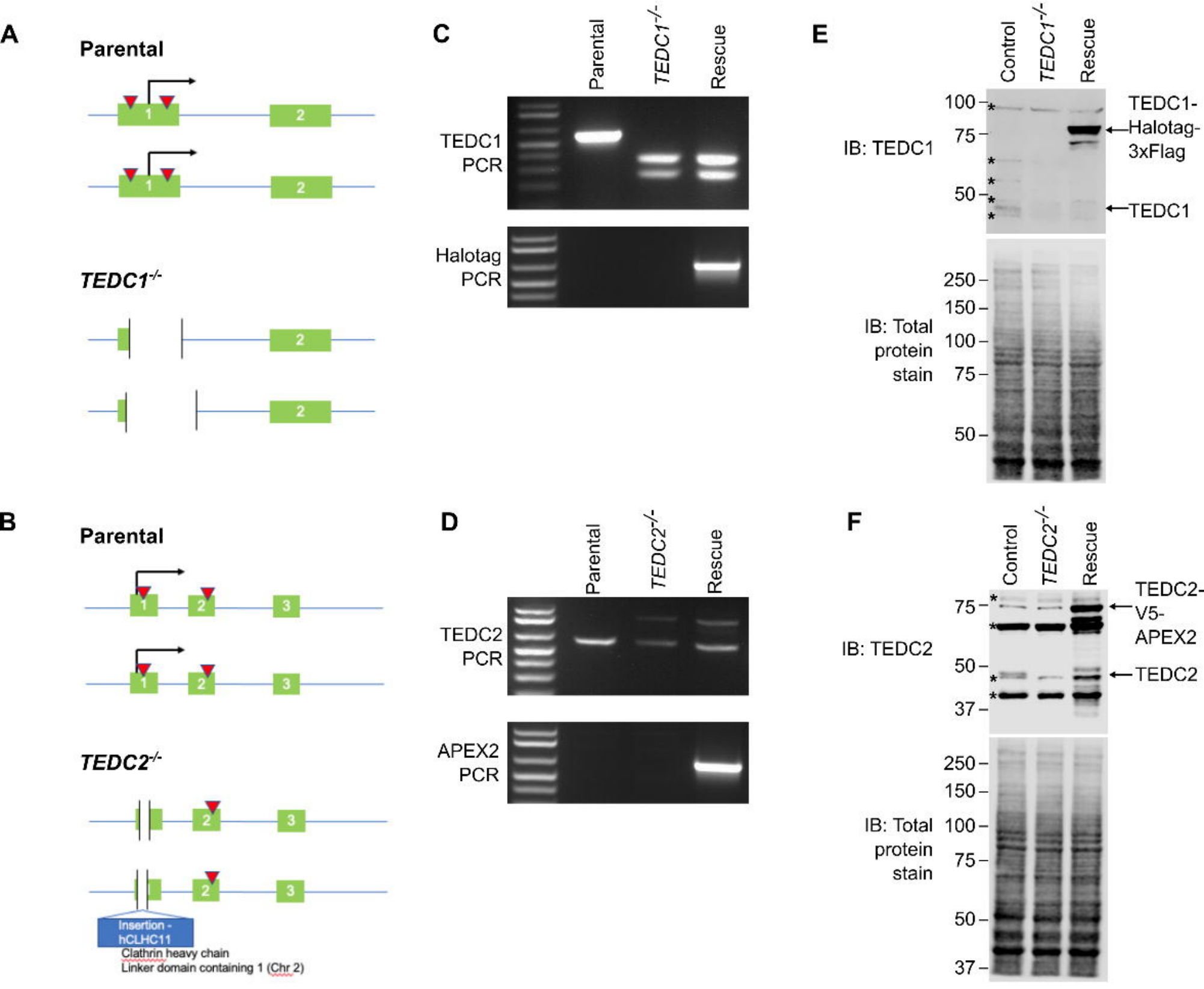

Fig 1 - Supp 2

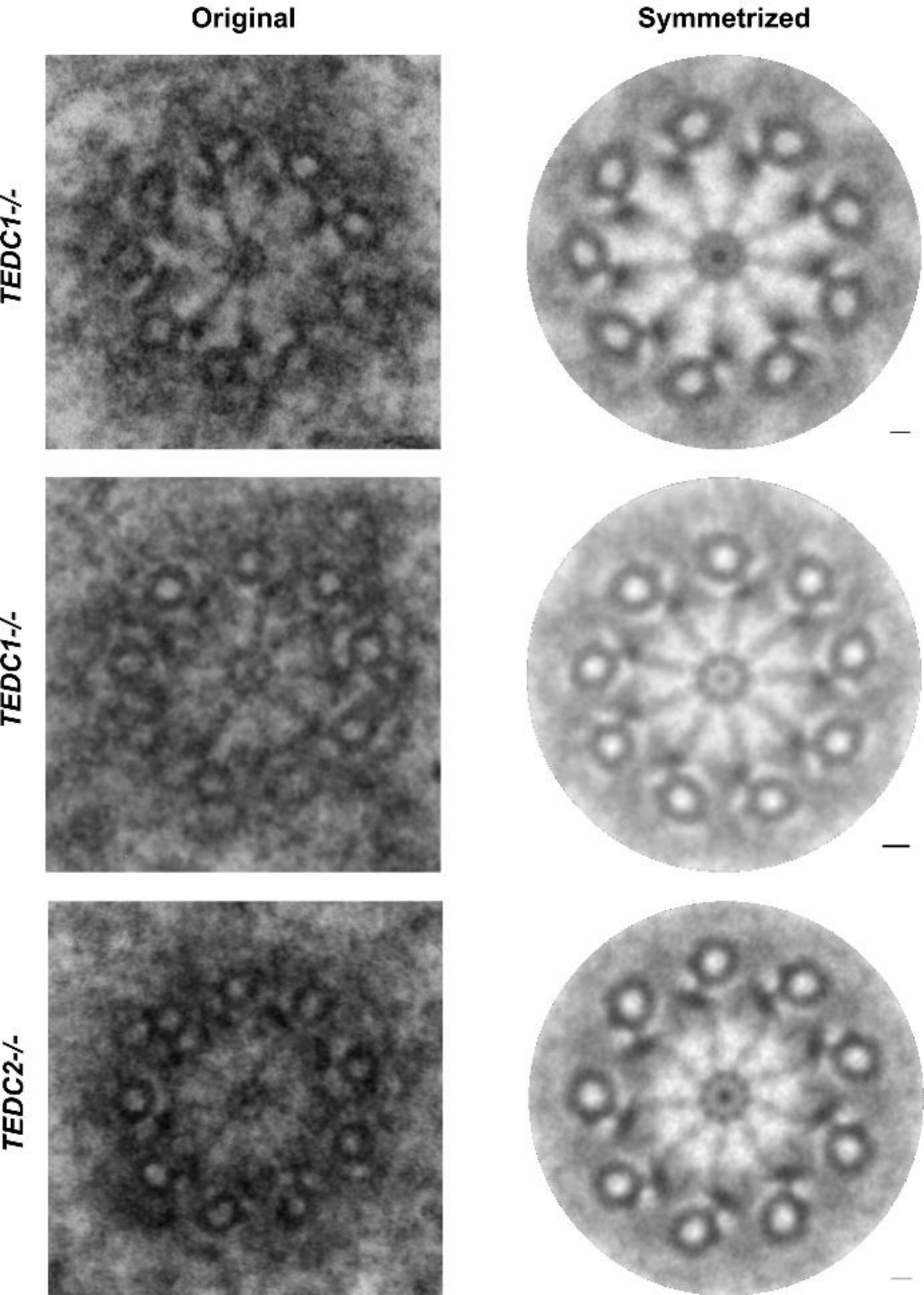

Figure 2

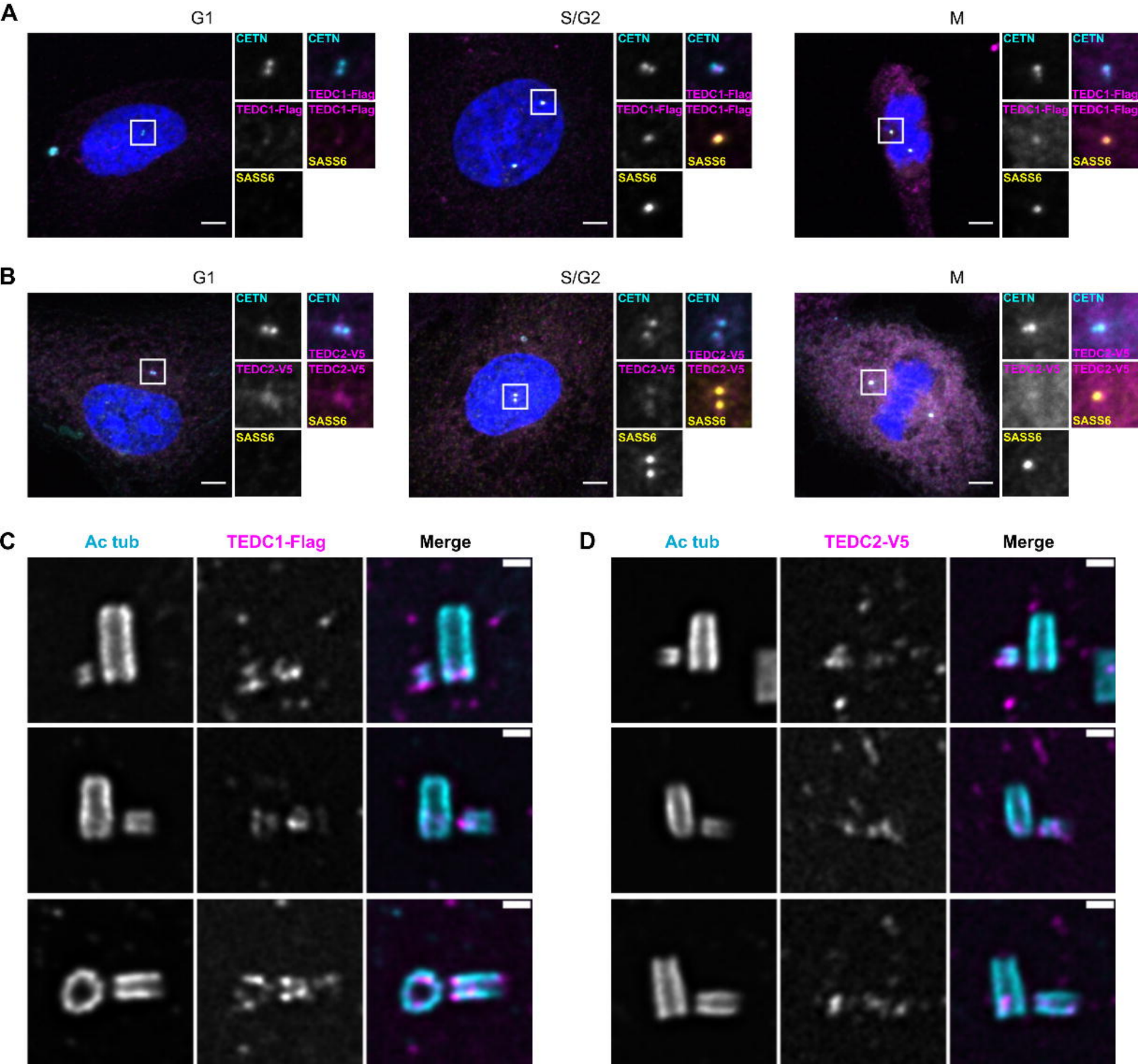

Figure 2 - Supp 1

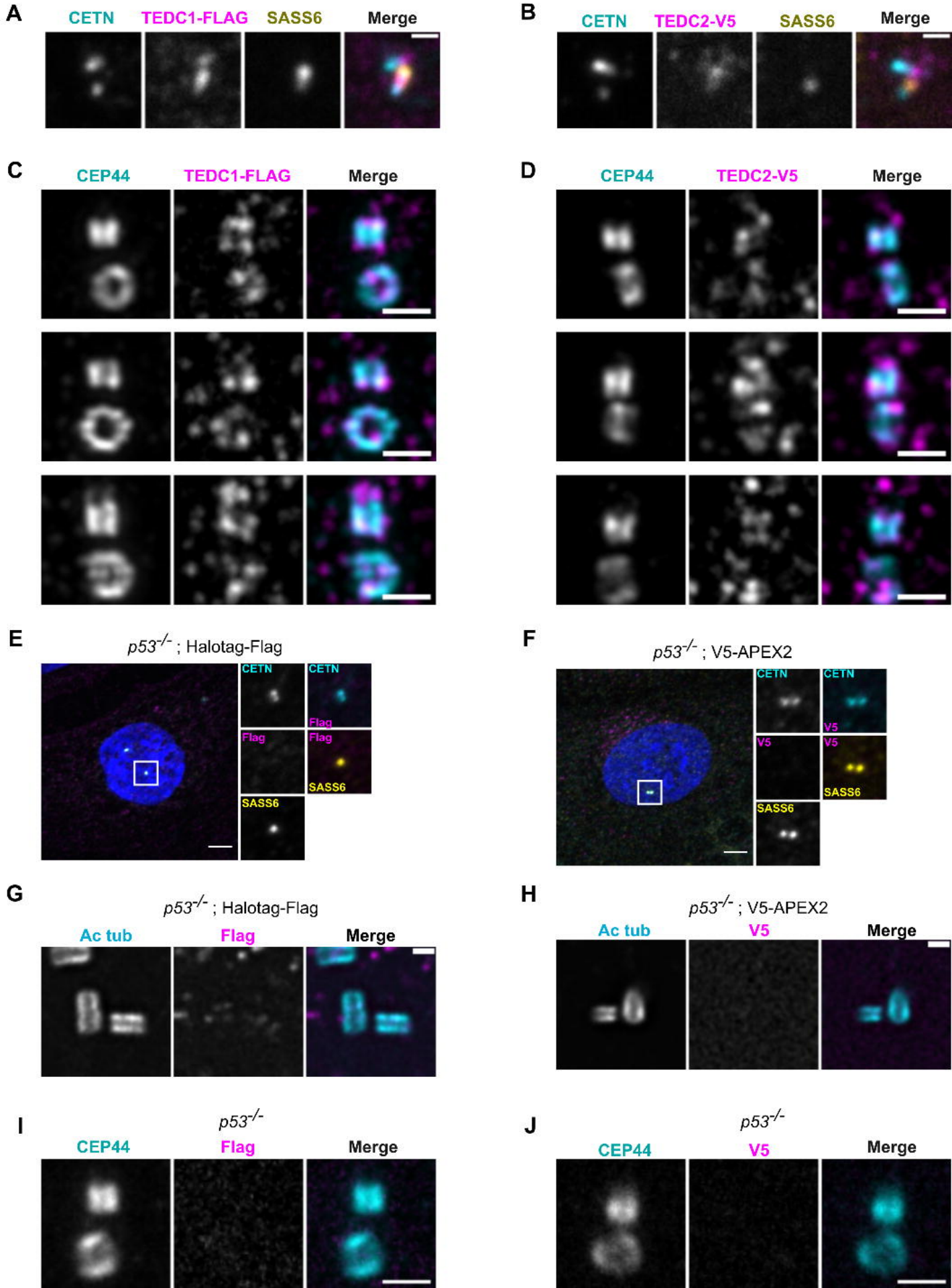

Figure 3

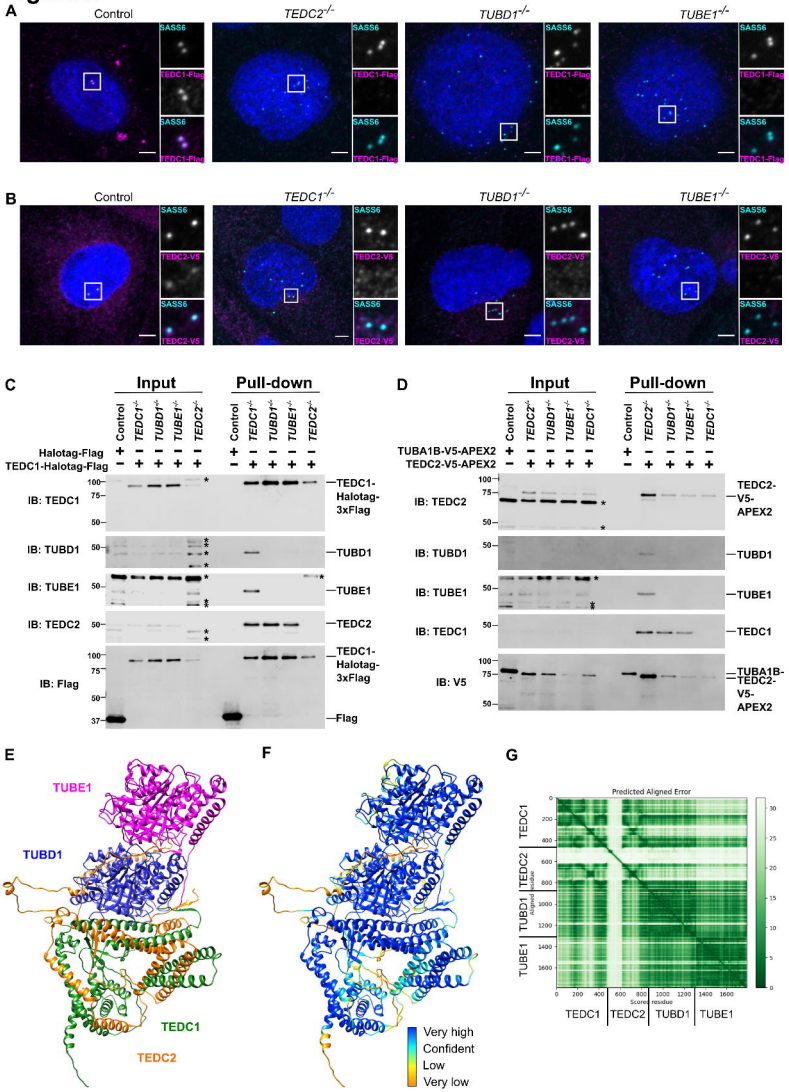
A
Control
TEDC2-/-
TUBD1-/-
TUBE1-/-
SASS6
TEDC1-Flag
B
TEDC2-V5
C
Input
Pull-down
Control
TEDC1-/-
TUBD1-/-
TUBE1-/-
TEDC2-/-
Halotag-Flag
TEDC1-Halotag-Flag
IB: TEDC1
IB: TUBD1
IB: TUBE1
IB: TEDC2
IB: Flag
TEDC1-Halotag-3xFlag
TUBD1
TUBE1
TEDC2
Flag
D
TUBA1B-V5-APEX2
TEDC2-V5-APEX2
IB: TEDC2
IB: TUBD1
IB: TUBE1
IB: TEDC1
IB: V5
TEDC2-V5-APEX2
TEDC1
TUBA1B-TEDC2-V5-APEX2
E
TUBE1
TUBD1
TEDC1
TEDC2
F
Very high
Confident
Low
Very low
G
Predicted Aligned Error
Aligned residue
Scored residue
TEDC1
TEDC2
TUBD1
TUBE1

Figure 3 - Supp 1

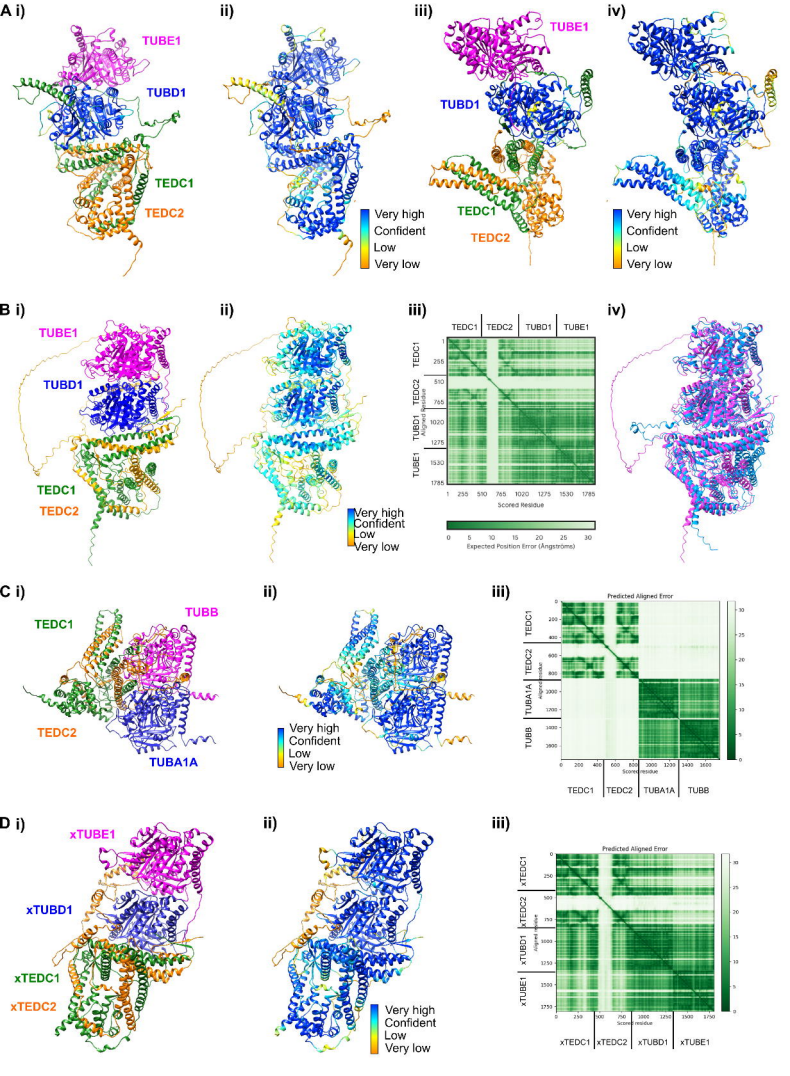

Figure 4

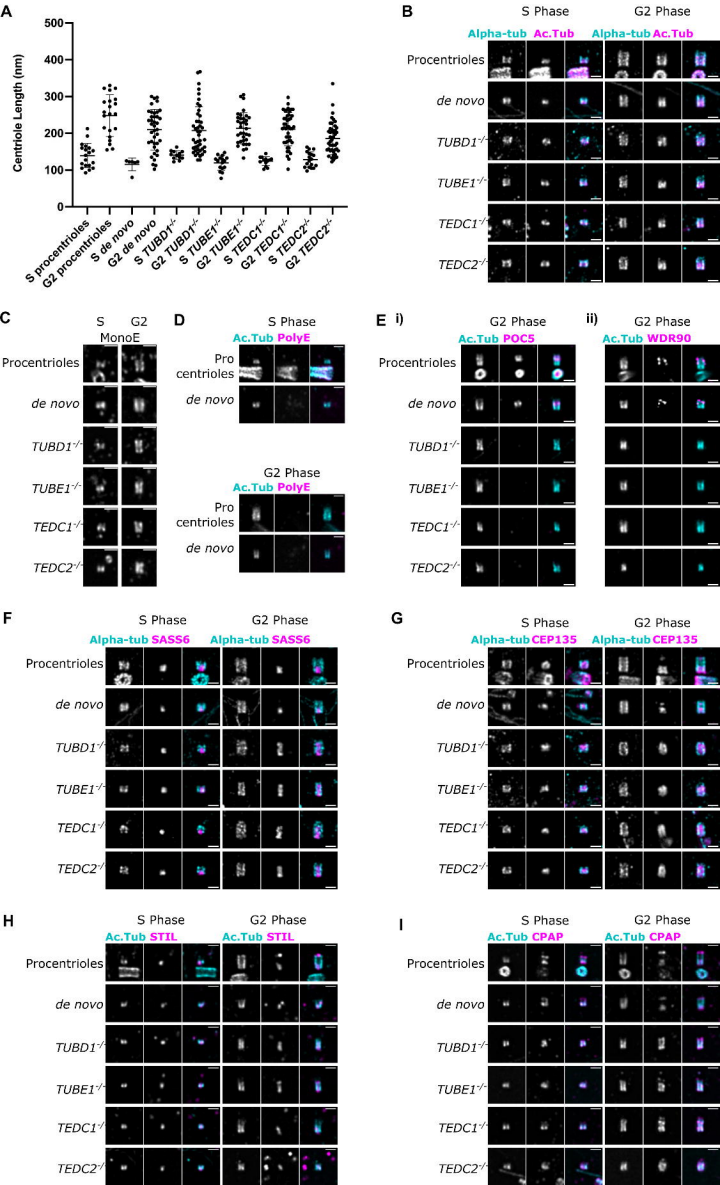
A
Centriole Length (nm)
500
400
300
200
100
0
S procentrioles
G2 procentrioles
S de novo
G2 de novo
S TUBD1-/-
G2 TUBD1-/-
S TUBE1-/-
G2 TUBE1-/-
S TEDC1-/-
G2 TEDC1-/-
S TEDC2-/-
G2 TEDC2-/-
B
S Phase
G2 Phase
Alpha-tub Ac.Tub
Alpha-tub Ac.Tub
Procentrioles
de novo
TUBD1-/-
TUBE1-/-
TEDC1-/-
TEDC2-/-
C
S
G2
MonoE
Procentrioles
de novo
TUBD1-/-
TUBE1-/-
TEDC1-/-
TEDC2-/-
D
S Phase
Ac.Tub PolyE
Pro centrioles
de novo
G2 Phase
Ac.Tub PolyE
Pro centrioles
de novo
E
i)
G2 Phase
Ac.Tub POC5
ii)
G2 Phase
Ac.Tub WDR90
Procentrioles
de novo
TUBD1-/-
TUBE1-/-
TEDC1-/-
TEDC2-/-
F
S Phase
G2 Phase
Alpha-tub SASS6
Alpha-tub SASS6
Procentrioles
de novo
TUBD1-/-
TUBE1-/-
TEDC1-/-
TEDC2-/-
G
S Phase
G2 Phase
Alpha-tub CEP135
Alpha-tub CEP135
Procentrioles
de novo
TUBD1-/-
TUBE1-/-
TEDC1-/-
TEDC2-/-
H
S Phase
G2 Phase
Ac.Tub STIL
Ac.Tub STIL
Procentrioles
de novo
TUBD1-/-
TUBE1-/-
TEDC1-/-
TEDC2-/-
I
S Phase
G2 Phase
Ac.Tub CPAP
Ac.Tub CPAP
Procentrioles
de novo
TUBD1-/-
TUBE1-/-
TEDC1-/-
TEDC2-/-

Figure 4 - Supp 1

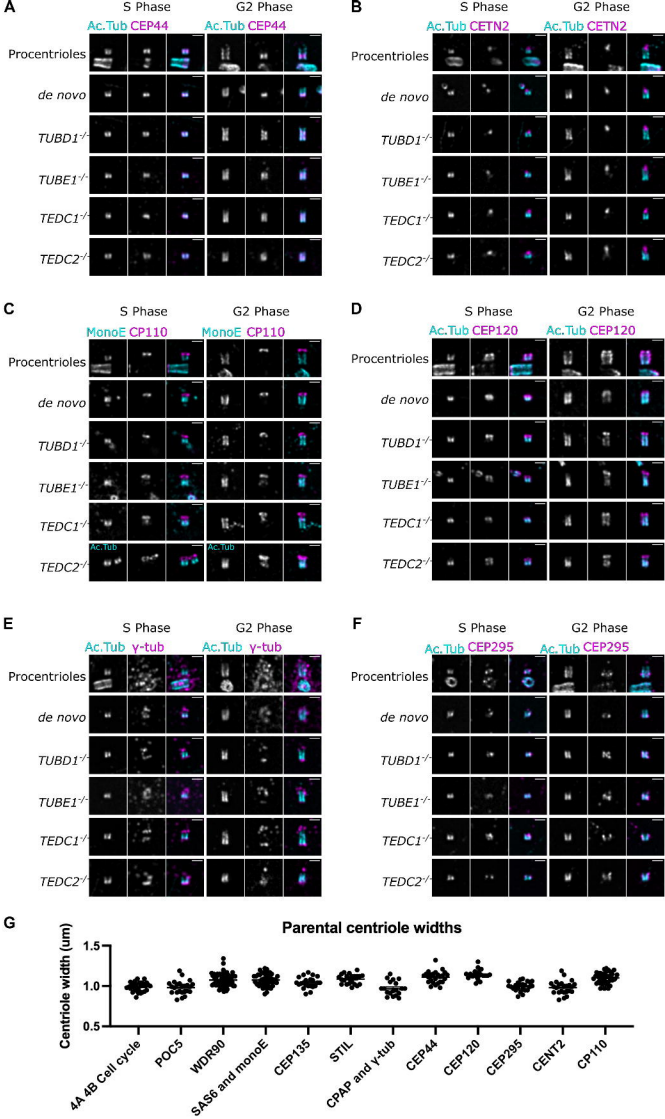

Figure 4 - Supp 2

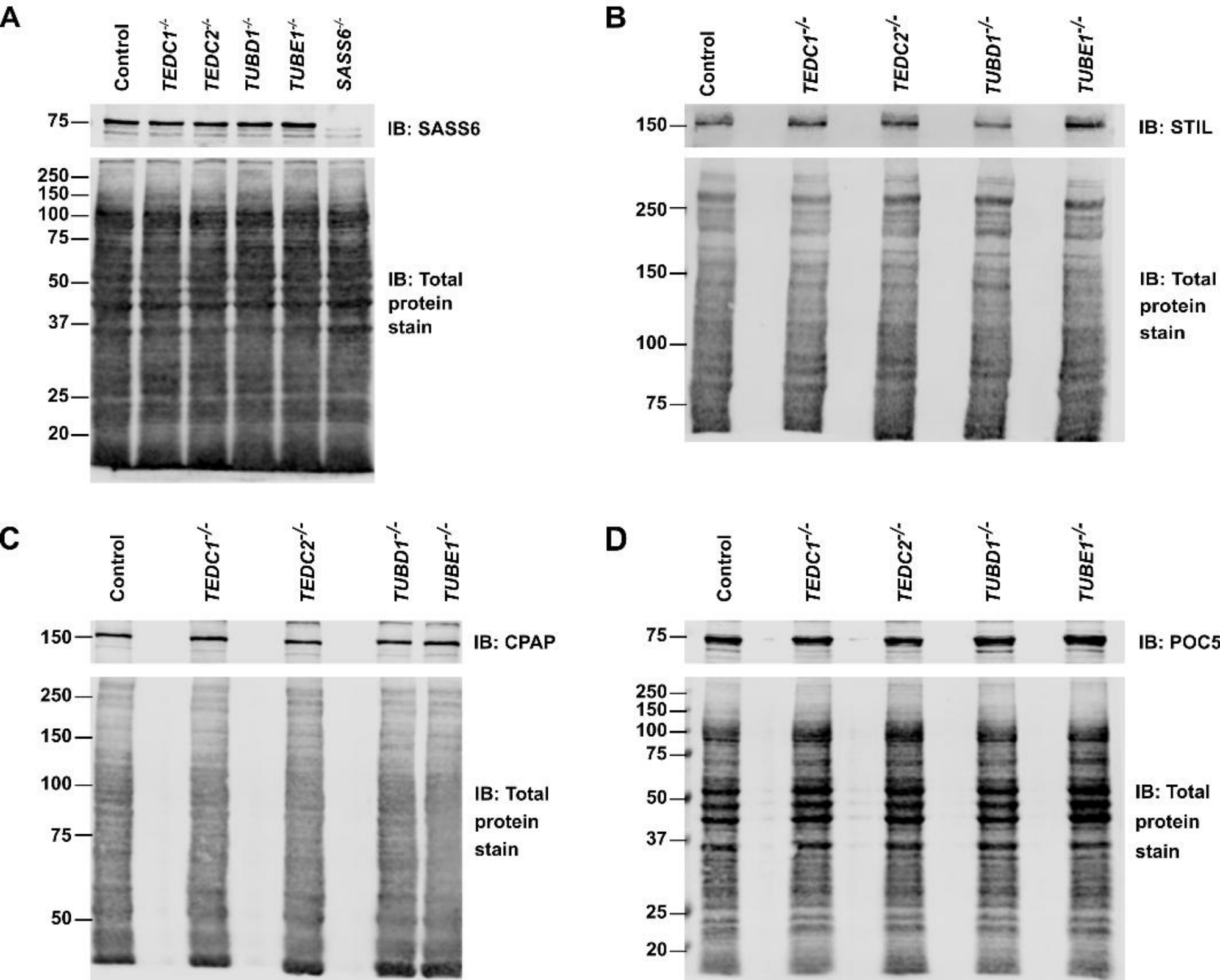

Figure 4 - Supp 3

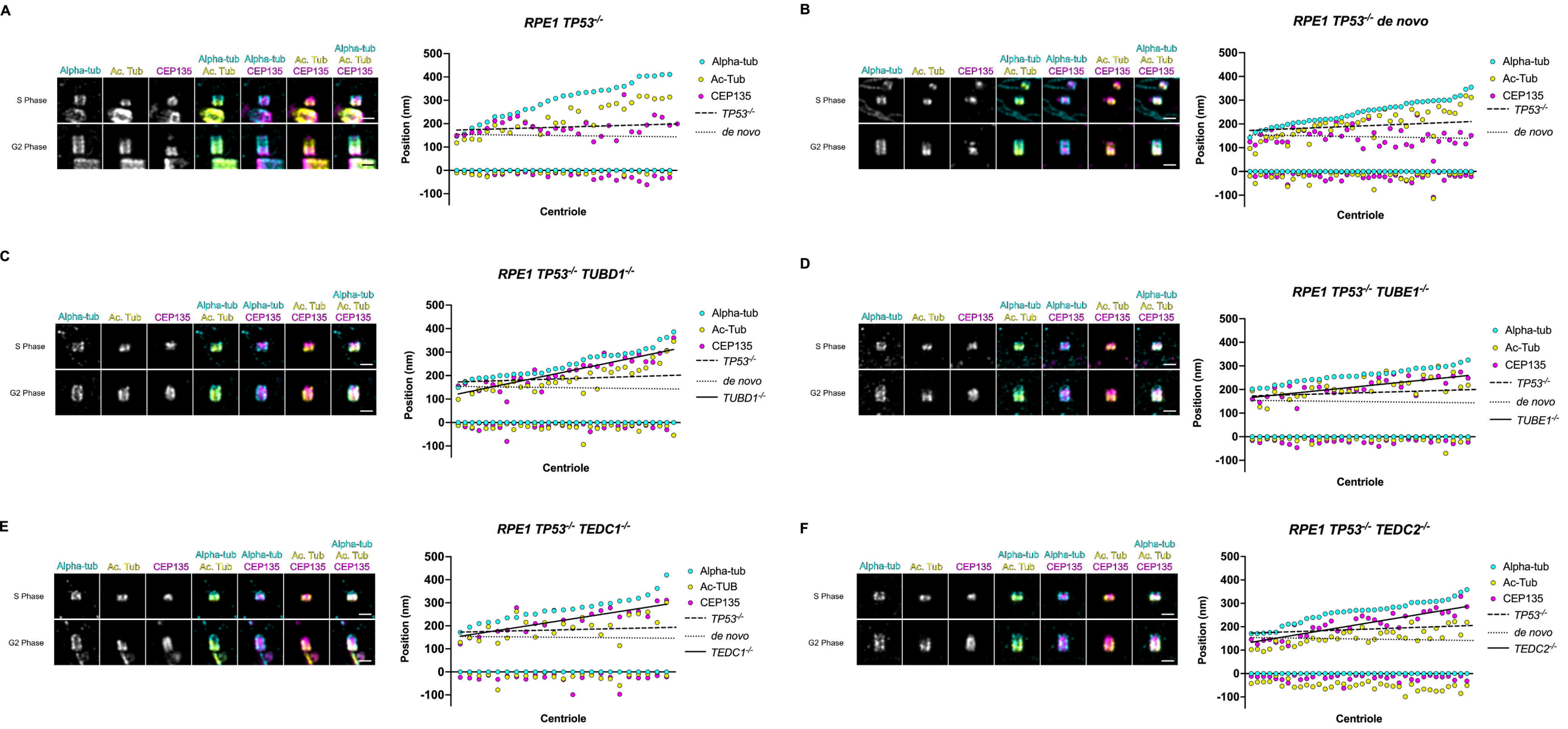

Fig 4 - Supp 4

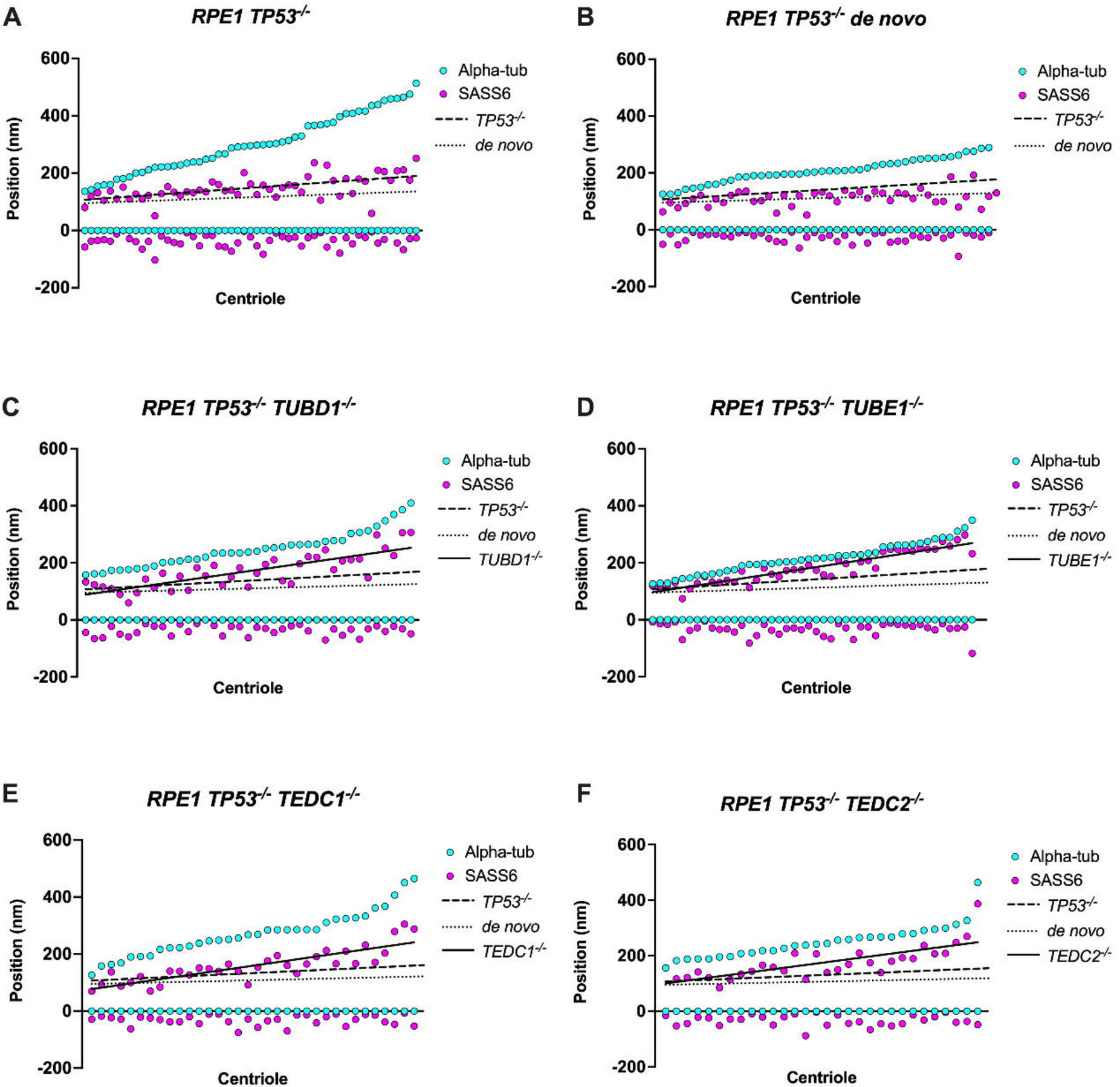
A
RPE1 TP53-/-
B
RPE1 TP53-/- de novo
C
RPE1 TP53-/- TUBD1-/-
D
RPE1 TP53-/- TUBE1-/-
E
RPE1 TP53-/- TEDC1-/-
F
RPE1 TP53-/- TEDC2-/-
Position (nm)
600
400
200
0
-200
Centriole
Alpha-tub
SASS6
TP53-/-
de novo
TUBD1-/-
TUBE1-/-
TEDC1-/-
TEDC2-/-

Fig 4 - Supp 5

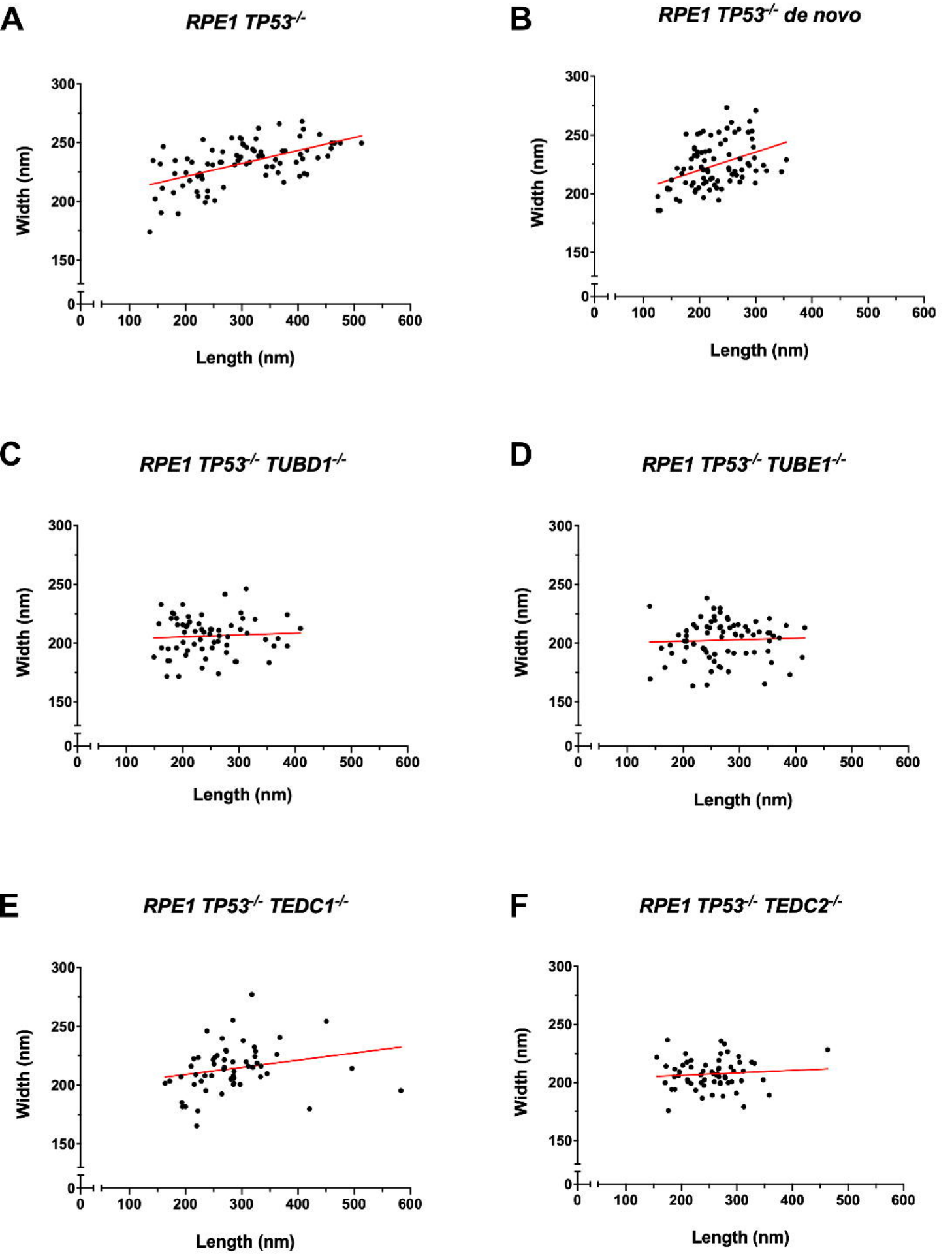
A
RPE1 TP53-/-
B
RPE1 TP53-/- de novo
C
RPE1 TP53-/- TUBD1-/-
D
RPE1 TP53-/- TUBE1-/-
E
RPE1 TP53-/- TEDC1-/-
F
RPE1 TP53-/- TEDC2-/-
Width (nm)
Length (nm)
0
100
150
200
250
300
400
500
600

Figure 5

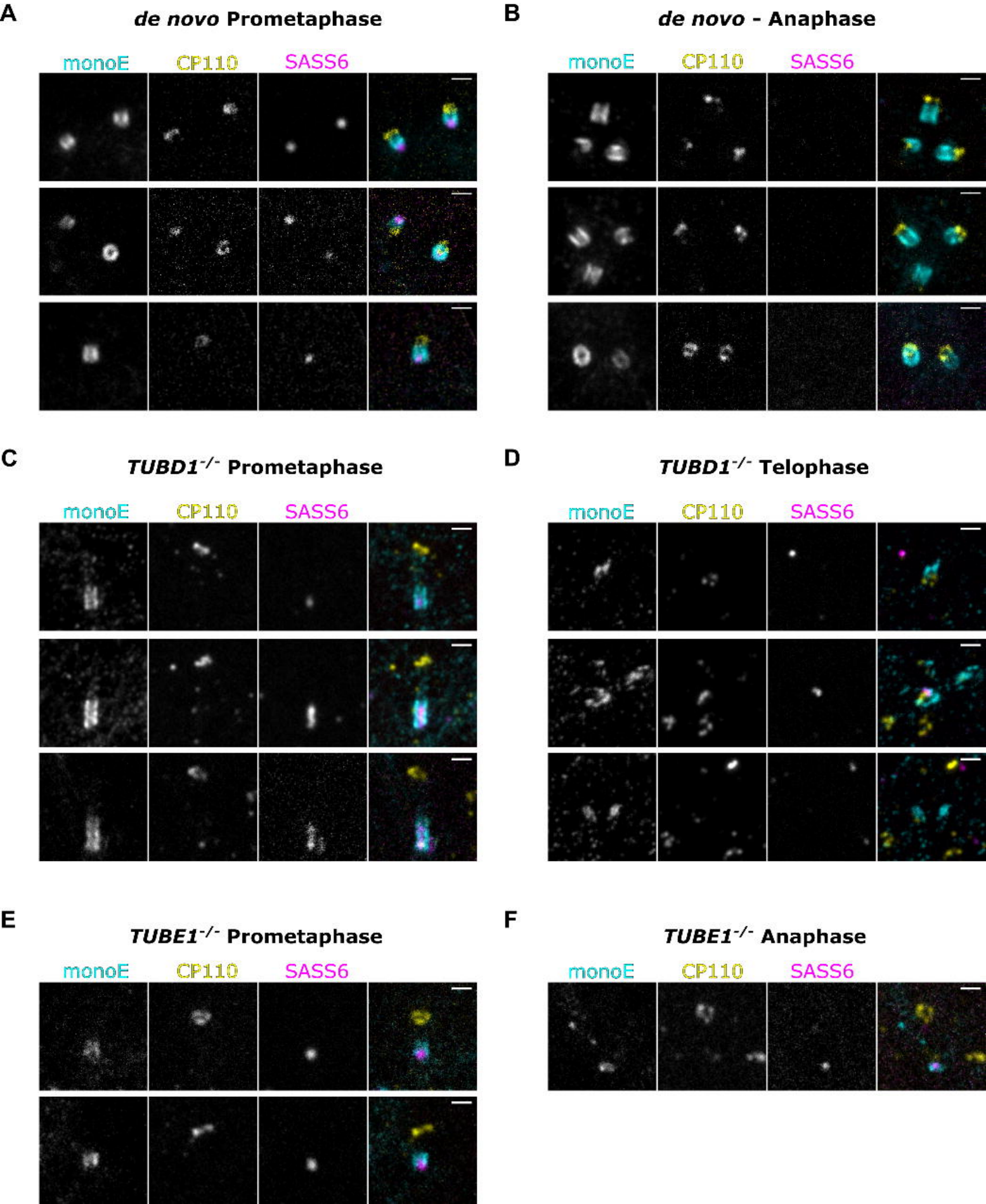
A
de novo Prometaphase
monoE
CP110
SASS6
B
de novo - Anaphase
monoE
CP110
SASS6
C
TUBD1-/- Prometaphase
monoE
CP110
SASS6
D
TUBD1-/- Telophase
monoE
CP110
SASS6
E
TUBE1-/- Prometaphase
monoE
CP110
SASS6
F
TUBE1-/- Anaphase
monoE
CP110
SASS6